Geochimica et Cosmochimica Acta 358 (2023) 12–26

Contents lists available at ScienceDirect

Geochimica et Cosmochimica Acta

journal homepage: www.elsevier.com/locate/gca

The magnesium isotopic composition of the mantle

Xiao-Ning Liu (刘效宁)[a,*], Remco C. Hin[a], Christopher D. Coath[a], Michael Bizimis[b], Li Su[c], Dmitri A. Ionov[d], Eiichi Takazawa[e], Richard Brooker[a], Tim Elliott[a]

[a] Bristol Isotope Group, School of Earth Science, University of Bristol, Bristol BS8 1RJ, UK
[b] School of Earth, Ocean and Environment, University of South Carolina, Columbia, SC 29208, USA
[c] Institute of Earth Sciences, China University of Geosciences, Beijing 100083, China
[d] Geosciences, Montpellier Université, Montpellier 34095, France
[e] Department of Geology, Faculty of Science, Niigata University, Niigata 950-2181, Japan

ARTICLE INFO

Associate editor: Tomas Magna

Keywords:
Mg isotopes
Mantle composition
Mg isotope fractionation factors
Critical mixture double-spiking

ABSTRACT

In order to better constrain the Mg isotopic composition of the mantle, we have analysed twenty-eight samples of both oceanic and continental peridotite using a high-precision, critical mixture double spiking approach. The unaltered samples show no variability δ^{26}Mg in outside analytical uncertainty and yield a value of -0.236 ± 0.006‰ (2 s.e.) for the accessible mantle, substantiating its non-chondritic composition. We have also determined inter-mineral Mg isotopic fractionations for a sub-set of samples. We document small but significant differences in δ^{26}Mg between olivine and pyroxenes, $\Delta^{26/24}\text{Mg}_{\text{ol/cpx}} = -0.118 \pm 0.018$‰ and $\Delta^{26/24}\text{Mg}_{\text{ol/opx}} = -0.056 \pm 0.018$‰, in excellent agreement with *ab initio* calculations for temperatures ~1000 °C, as recorded by mineral thermometry in the peridotites. The differences in δ^{26}Mg between olivine and spinel ($\Delta^{26/24}\text{Mg}_{\text{ol/sp}}$) are more variable and generally higher than theoretical calculations at corresponding temperatures, likely due to incomplete Fe-Mg diffusive exchange during post-eruptive cooling of the xenoliths.

Using these data, together with a recently determined olivine-melt fractionation factor for Mg isotopes, we show that partial melting has a negligible influence on the δ^{26}Mg of residual peridotites. This helps account for the minimal variability of δ^{26}Mg in fresh, mantle peridotites. However, the δ^{26}Mg of primary mantle melts are predicted to be discernibly higher than their sources (Δ^{26}Mg ~ 0.06‰ and ~0.123‰ for representative partial melts of peridotitic and pyroxenitic sources respectively) across a wide range of melting conditions. Such elevated δ^{26}Mg values are not generally observed in the current dataset of mantle derived melts. We propose that this inconsistency is likely a consequence of diffusive fractionation during partial re-equilibration between low Mg/Fe melts migrating through high Mg/Fe mantle en route to the surface.

1. Introduction

The Mg isotope system has been used as a powerful tracer of several major processes in terrestrial evolution. A subtle difference between the magnesium isotopic composition of the bulk mantle and chondritic meteorites has been used to infer ~40% mass loss by vaporisation during the accretion of the Earth (Hin et al., 2017). Several studies have modelled potentially discernible differences in the Mg isotopic composition of melts produced from pyroxenitic and peridotitic sources (Zhong et al., 2017; Stracke et al., 2018; Wang et al., 2020; Soderman et al., 2022), providing a much sought after means of identifying such lithological heterogeneity. The marked isotopic fractionation of Mg incorporated into carbonate structures further holds significant promise in tracing the fate of carbonate subducted into the mantle (e.g., Wang et al., 2018). All of these applications require a well-defined Mg isotopic composition of the bulk mantle.

Much effort has already been expended in constraining this value through peridotite analyses (Handler et al., 2009; Yang et al., 2009; Bourdon et al., 2010; Teng et al., 2010; Huang et al., 2011; Liu et al., 2011; Pogge von Strandmann et al., 2011; Xiao et al., 2013, 2016; Lai et al., 2015; Wang et al., 2016; An et al., 2017; Stracke et al., 2018; Hu et al., 2020) and these sample-standard bracketing measurements yield a typical value of $\delta^{26}\text{Mg}_{\text{DSM}}$ (the relative difference of $^{26}\text{Mg}/^{24}\text{Mg}$ ratio of sample from reference material DSM-3, Galy et al., 2003) around −0.25‰ for 'normal' mantle (Teng, 2017). The improved reproducibility achievable using critical mixture double-spiking (Coath et al.,

* Corresponding author.
E-mail address: xiaoning.liu@bristol.ac.uk (X.-N. Liu).

https://doi.org/10.1016/j.gca.2023.08.011
Received 25 December 2022; Accepted 8 August 2023
Available online 11 August 2023

2017; Hin et al., 2017; He et al., 2022), however, prompts a reassessment of mantle Mg isotopic compositions. Hin et al. (2017) analysed a range of peridotites using critical mixture double spiking but their datum of mantle δ^{26}Mg was based on a rather limited number of samples from the continental lithosphere mantle alone. Thus, we have carefully chosen twenty-eight mantle peridotites, including the samples of the oceanic lithosphere, to test with a more substantial dataset the proposed minimally variable and non-chondritic magnesium isotopic composition of the Earth's mantle (Hin et al., 2017).

Interpreting the information carried in the Mg isotopic compositions of mantle derived melts further requires accurate and precise fractionation factors between mantle phases (e.g., Soderman et al., 2022). Measurements of mineral separates from peridotites have provided vital empirical support of magnesium isotopic fractionation factors determined from theory (Handler et al., 2009; Yang et al., 2009; Liu et al., 2011; Huang et al., 2011; Pogge von Strandmann et al., 2011; Xiao et al., 2013, 2016; Lai et al., 2015; Hu et al., 2016; An et al., 2017; Liu et al., 2017; Zhao et al., 2017; Chen et al., 2018; Stracke et al., 2018; Hu et al., 2020). Yet the inter-mineral fractionations are subtle compared to the typical analytical reproducibility of sample-standard bracketing analysis, so the *ab initio* calculations have not currently been calibrated to appropriate precision. We have addressed this issue by measuring Mg isotopic differences, by critical mixture double-spiking, in twenty-one mineral pairs from six peridotite samples.

Finally, a well constrained mantle δ^{26}Mg and robust inter-mineral fractionations can be coupled with a recently determined, high precision olivine-melt fractionation factor (Liu et al., 2022) to predict the compositions of mantle derived melts. Previous calculations (Zhong et al., 2017; Stracke et al., 2018; Wang et al., 2020; Soderman et al., 2022) suggested mantle derived melts could have Mg isotopic compositions fractionated from their sources by ~0.03–0.1‰. Yet uncertainty in the fractionation factors available to these studies results in inconsistent predictions. Thus, we re-evaluate likely Mg isotopic variations in primary melts and compare these model results with literature data (e.g., Teng et al. 2010).

2. Samples

We analysed peridotites from diverse geological settings that encompass well characterised geochemical differences in the mantle (Table 1, Fig. 1). Secondary alteration can significantly fractionate the Mg isotopic ratios of peridotite samples (Beinlich et al., 2014; Liu et al., 2017; Zhao et al., 2023), so our focus is on the freshest samples. We selected samples with low loss on ignition (LOI), typically <0.5 wt% (Table 1). For samples from which we hand-picked mineral fragments, we only analysed optically clear phases, most critical for olivines (see Fig. 2a and b). To gauge the influence of alteration, however, we also analysed one sample (BZ-26 from Zabargad) which was visually not pristine (Fig. 2c), contained abundant fluid inclusions and is our only sample with LOI > 1 wt%.

We analysed whole-rock powders of nine mantle xenoliths of off-craton, continental lithosphere from Tariat, Mongolia (Preß et al., 1986; Stosch et al., 1986; Ionov, 2007; Ionov and Hofmann, 2007; Carlson and Ionov, 2019) and Vitim, southern Siberia (Ionov, 2004, Ionov et al., 2005). These samples include some notably fertile peridotitic compositions (Fig. 1a). We selected samples recovered from rapidly cooled tuff deposits to avoid potential kinetic fractionations that may occur during slower cooling of lava flow hosted xenoliths (Pogge von Strandmann et al., 2011).

Four of our sample localities are grouped as continental-oceanic transition in Table 1. Included in this group are six orogenic peridotite samples from the Horoman and Twin Sister massifs, the latter represented by international rock standard DTS-2. The Horoman peridotite has been argued to be formed from ancient (0.8–1 Ga) partial melting residues of a MORB source mantle (Takazawa et al., 1996; 2000; Yoshikawa and Nakamura, 2000; Saal et al., 2001; Malaviarachchi et al., 2008, 2010), which then reacted with percolating melt at ~23 Ma, possibly in a mantle wedge environment, locally causing the enrichment in LREE and the rare formation of phlogopite (Yoshikawa et al., 1993; Takazawa et al., 1996). Lai et al. (2015) identified some Horoman samples that have kinetically perturbed Li isotopic ratios. We avoided analysing these samples for high precision Mg isotope measurements. We further analysed two samples from the Zabargad massif, Red Sea (Brooker et al., 2004), the evolution of which is more contentious. Although it has most recently experienced processes in a rift setting (e.g., Dupuy et al., 1991), a complex, earlier history has been proposed (e.g., Brueckner et al., 1995), including a subduction influence (Brooker et al., 2004). A mantle wedge environment is more definitively sampled by two xenoliths from Avacha in the active Kamchatka Island arc (Ionov and Seitz, 2008; Ionov, 2010; Ionov et al., 2011; Bénard et al., 2017).

We measured five, clearly intra-oceanic, mantle xenoliths from Oahu, Hawaii. Four are from Salt Lake Crater (SLC) and one is from the Pali vents near the rim of the Koolau crater (Sen, 1988; Sen et al., 1993; Bizimis et al., 2004, 2007). The SLC peridotites have highly unradiogenic Os (with Re depletion ages up to 2 Ga) and radiogenic Hf isotope signatures. These xenoliths represent fragments of ancient mantle lithosphere embedded in the Hawaii mantle plume (Bizimis et al., 2007). In this context, the SLC xenoliths provide a valuable opportunity to sample hotspot mantle. In contrast, the Pali sample is derived from the current Pacific lithosphere beneath Hawaii (Bizimis et al., 2007). We characterised the Hawaii xenoliths using analyses of hand-picked minerals rather than whole rock powders, which enables us to examine inter-mineral fractionations, as well as numerically reconstruct their bulk compositions.

The equilibration temperatures of the Hawaii xenoliths were determined using a variety of different thermometers involving different mineral equilibria: the Fe-Mg exchange two-pyroxene thermometer, T_{BKN} (Brey and Köhler, 1990), thermometer of Na partitioning between orthopyroxene and clinopyroxene, $T^{Na}{}_{Opx\text{-}Cpx}$ (Brey and Köhler, 1990), olivine trace element thermometer, T_{Ol} (De Hoog et al., 2010) and the thermometer of Al partitioning between olivine and spinel, $T^{Al}_{Ol\text{-}Sp}$ (Wan et al., 2008). Temperatures calculated using T_{BKN}, $T^{Na}_{Opx\text{-}Cpx}$ and T_{Ol} are in agreement with each other, ranging from ~900 to ~1050 °C for the five Hawaii xenolith samples, while the temperatures of $T^{Al}_{Ol\text{-}Sp}$ are inconsistent with others (Fig. 3). These observations demonstrate equilibrium between olivine, clinopyroxene and orthopyroxene, while the spinel is not fully equilibrated with other minerals (also see section 5.2 about disequilibrium between olivine and spinel).

The oceanic upper mantle is further represented by four peridotite samples from Zedang, Xigaze and Pulan ophiolites, that form part of the Tibetan Yarlung Zangbo ophiolite belt (Bao et al., 2013, 2014). The Tibetan Yarlung Zangbo ophiolite peridotite samples are unusually well-preserved (e.g., Malpas et al., 2003; Hébert et al., 2012) and we selected bulk samples with LOI < 0.5 wt%. For these samples we worked on rock chips from which we hand-picked fresh olivines (Fig. 2b).

In all, the selected peridotites range from near fertile to strongly melt-depleted with Mg# from 88.7 to 92.0 and coupled variations in Al_2O_3 contents from 4.32 to 0.44 wt% (Fig. 1a). Samples show variable metasomatic influence, with primitive mantle normalised La/Sm ($[La]_{PM}/[Sm]_{PM}$) ranging from 0.2 to 6.3 (Fig. 1b). Our dataset thus covers a wide range of mantle compositional variability as well as tectonic setting.

3. Methods

3.1. Critical mixture double spike technique

Details of the theory and application of critical mixture double-spiking have been described by Coath et al. (2017), Hin et al. (2017) and Liu et al. (2022), but a synopsis is given here as the technique remains little exploited, with only one other group outside Bristol reporting such data to date (He et al., 2022). We also provide detailed

Table 1
Magnesium isotopic compositions of bulk mantle peridotites measured by critical mixture double-spiking. Samples grouped by tectonic setting and accompanied by key compositional data from the literature (see main text for references).

Sample ID	Rock type	Al_2O_3 (wt.%)	MgO (wt.%)	Mg# (%)	$[La]_{PM}/[Sm]_{PM}$	LOI (wt.%)	$\delta^{26}Mg$	Pooled 2 s.e.	N
Continental (off-craton)									
Xenoliths from Tariat, Mongolia									
H25	Sp-Harzburgite	0.62	47.75	91.8	2.40	−0.44	−0.239	0.022	6
Mo4230-16	Pl-Sp-Lherzolite	4.32	38.80	88.7		0.31	−0.238	0.022	6
S16	Sp-Lherzolite	3.04	41.16	90.3	4.42	−0.40	−0.231	0.022	6
S1	Sp-Lherzolite	4.27	37.19	89.1	0.44	−0.47	−0.213	0.038	4
S2	Sp-Lherzolite	3.86	38.59	89.4	1.02	−0.36	−0.219	0.022	6
replicate							−0.220	0.030	4
average							−0.219	0.018	10
S62	Sp-Lherzolite	1.74	44.04	91.3	3.06	−0.31	−0.223	0.022	6
Xenoliths from Vitim, southern Siberia, Russia									
313–105	Gar-Lherzolite	3.23	40.37	89.9	0.92	0.32	−0.259	0.034	5
313–240	Gar-Lherzolite	3.25	40.17	89.2	1.56	0.27	−0.227	0.034	5
314–58	Sp-Lherzolite	3.76	38.58	89.3	0.58	0.25	−0.224	0.034	5
313–102[#1]	Gar-Lherzolite	4.76	37.05	88.4	1.14	0.08	−0.254	0.020	
Continental-Oceanic transition									
Zabargad massif, Red Sea, Egypt									
BZ-230	Sp-Lherzolite	3.71	38.39	89.0	0.25	0.84	−0.215	0.038	4
BZ-26	Sp-Lherzolite	2.11	40.97	90.3	0.72	1.04	−0.151	0.022	6
BZ-26[#2]							−0.170	0.035	
BZ-29[#1]	Sp-Lherzolite	3.81	38.13	88.9	0.45	0.58	−0.225	0.020	
Horoman massif, Hokaido, Japan									
BZ117	Sp-Harzburgite	0.78	45.46	91.4	0.90		−0.244	0.034	5
BZ131	Sp-Harzburgite	0.56	45.88	91.3			−0.214	0.034	5
BZ134	Sp-Lherzolite	1.42	44.43	91.3	0.18		−0.253	0.038	4
BZ252	Pl-Lherzolite	3.53	38.70	89.5	0.17		−0.237	0.038	4
JP-1	Harzburgite	0.66	44.60	91.5	2.78		−0.223	0.010	53
BZ251[#1]	Pl-Lherzolite	3.18	39.43	89.9	0.14	0.50	−0.252	0.020	
BZ143[#1]	Sp-Lherzolite	2.04	42.24	90.4	0.28		−0.235	0.018	
BZ116[#1]	Sp-Harzburgite	0.50	46.21	91.2			−0.260	0.018	
Twin Sisters massif, Oregon, USA									
DTS-2	Dunite	0.44	49.67	92.0	2.30	0.36	−0.269	0.023	10
Xenoliths from Avacha, Kamchatka peninsula, Russia									
Av6	Sp-Harzburgite	0.48	45.97	90.9	1.36	0.65	−0.254	0.029	6
Av33	Sp-Harzburgite	0.66	44.69	90.6		−0.50	−0.225	0.029	6
Oceanic									
Xenoliths from Oahu, Hawai, USA									
77SL405[#2]	Sp-Lherzolite	2.10	42.95	90.1	1.48		−0.190	0.020	
77SL466[#2]	Sp-Lherzolite	3.19	41.24	89.8	0.97		−0.257	0.020	
77SL470[#2]	Sp-Lherzolite	1.23	43.60	91.3	1.73		−0.229	0.020	
88PAL12[#2]	Sp-Lherzolite	2.89	39.67	90.2	1.44		−0.240	0.020	
11504826[#2]	Sp-Lherzolite	2.00	43.42	90.5	0.52		−0.265	0.020	
Yarlung Zangbo ophiolite, Tibet, China									
ZN-10[#3]	Sp-Lherzolite	1.87	42.54	90.5	0.76	0.10	−0.242	0.027	
ZB-87[#3]	Sp-Lherzolite	1.60	42.92	90.6	6.33	−0.08	−0.219	0.027	
TB-93[#3]	Sp-Lherzolite	1.40	44.12	91.0	1.76	0.38	−0.248	0.027	
TB-157[#3]	Sp-Harzburgite	0.74	44.68	91.0	0.74	0.41	−0.246	0.027	
Mean value*							**−0.236**	**0.006**	

N is the number of individual measurements (see section 3.2) that comprise the reported mean $\delta^{26}Mg$.
$[La]_{PM}/[Sm]_{PM}$ values for the Hawaii samples are those on clinopyroxenes, the rest are bulk-rock data.
[#1] From Hin et al. (2017), recast from $\delta^{25}Mg$ into $\delta^{26}Mg$ by $\delta^{26}Mg = \delta^{25}Mg \times 1.9569$.
[#2] Calculated from the individual mineral Mg isotopic composition.
[#3] Estimated from the olivine Mg isotopic composition.
* BZ-26 is excluded.

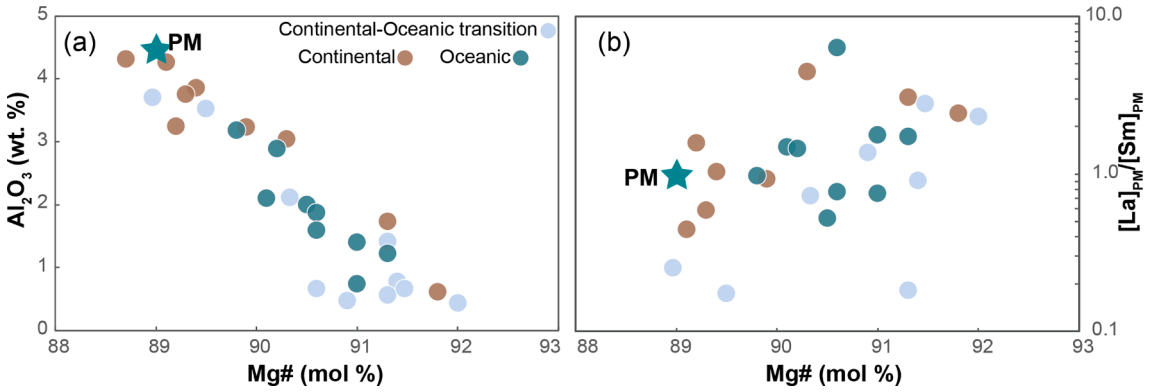

Fig. 1. Geochemical variations of the peridotite samples analysed in this study. (a) Bulk Mg# (mol%) versus bulk Al_2O_3 (wt.%) and (b) bulk Mg# versus the primitive mantle (PM) normalised La/Sm ratio. Primitive mantle composition after Palme and O'Neill (2014). Samples are grouped according to tectonic setting: 'Continental' includes samples from Tarit and Vitim, 'Continental-Oceanic transition' includes samples from Horoman, Twin Sister, Avacha and Zabargad, and 'Oceanic' includes samples from Hawaii and Tibet.

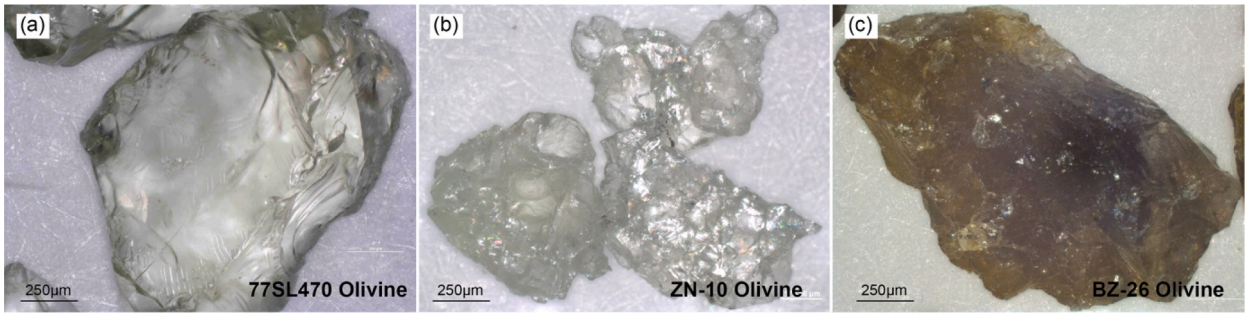

Fig. 2. Images of example olivine grains under the optical microscope from (a) Hawaiian xenolith 77SL470 (Fo content 91.2), (b) Tibetan ophiolite ZN-10 (Fo content 90.6) and (c) Zabargad peridoite BZ-26 (Fo content 90.3). 77SL470 and ZN-10 do not have any signs of alteration, while the BZ-26 is obviously altered, with dark-brown olivine grains.

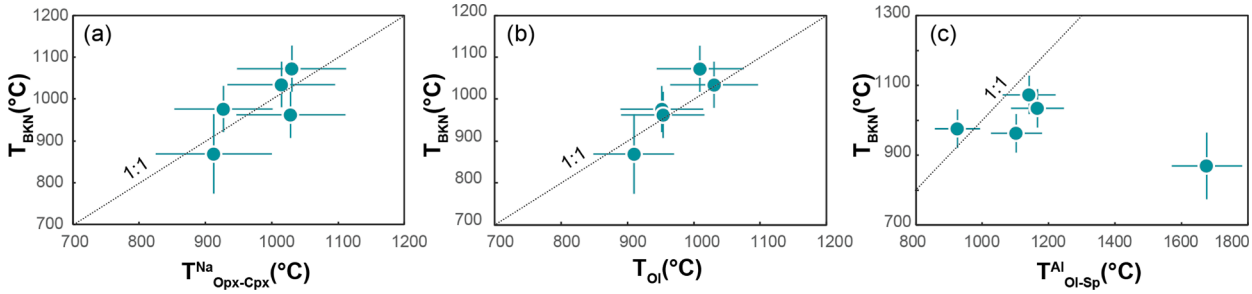

Fig. 3. The comparison of the equilibration temperature calculated from different thermometers involving different mineral equilibria. (a) Between two pyroxene thermometer (T_{BKN}) and Na partitioning thermometer ($T^{Na}_{Opx\text{-}Cpx}$); (b) between two pyroxene thermometer (T_{BKN}) and olivine trace element thermometer (T_{Ol}); (c) between two pyroxene thermometer (T_{BKN}) and Al partitioning thermometer ($T^{Al}_{Ol\text{-}Sp}$). Error bars are estimated based on the ±1% (relative error) element content uncertainty in each mineral.

protocols of the critical mixture double-spiking Mg isotope analysis in the supplementary material. The impetus for this approach is that the alternative sample-standard bracketing approach relies on external normalisation to correct for instrumental fractionation based on the assumption that samples and standards behave identically during analysis; since separation of elements during sample preparation is never perfect, this condition is never strictly met. Inaccuracy stems from different amounts of residual matrix in different samples and its influence on the transmission of analyte ions under different plasma and focussing conditions (e.g., Teng and Yang, 2014). Such instrumental mass bias cannot be resolved from natural isotopic variability. The uncertainty on an individual measurement therefore does not reflect long term reproducibility, because of session-to-session changes in plasma conditions. Thus, using the standard error of multiple analyses provides an unreliable estimate of the precision of a measurement and uncertainty is typically assessed by the long-term standard deviation of repeat measurements (Teng and Yang, 2014; Teng et al., 2015a; Teng, 2017). This is a significant limitation on the precision of Mg isotope measurements given Mg is a major element and there is typically sufficient material to permit much higher precisions from counting statistics.

A more robust way to normalise instrumental mass fractionation is the double-spiking technique, whereby a known mixture of two purified isotope spikes is added to a sample. This technique explicitly corrects for instrumental mass-bias during analysis. Using three equations and three measured isotope ratios, three unknowns are simultaneously calculated (sample natural fractionation, α, instrumental fractionation, β, and spike

proportion, p) to provide accurate isotope ratio measurements (e.g., Dodson, 1963; Albarède and Beard, 2004; Rudge et al., 2009).

Since the double-spike technique needs at least four isotopes to provide three independent isotope ratios as inputs to solve the three unknowns, it is not obviously accessible to three-isotope systems such as Mg. However, Coath et al. (2017) developed the idea of a "critical mixture", first used by Hofmann (1971), to apply the double-spiking approach to a system with only three stable isotopes. The critical mixture is a unique composition that lies on a mixing line between natural and spike compositions in three-isotope space where the slope of this mixing line coincides with the slope of the tangent to the mass-bias fractionation curve. For such a critical mixture, $d\alpha/d\beta = 0$ (Coath et al., 2017) and so any deviation of β will not contribute, to first order, to the variation of α, i.e., determination of the natural isotope ratio is largely unaffected by inaccuracy or variability in instrumental mass bias. An initial estimate of the instrumental fractionation β thus suffices for α to be accurately determined in a critical mixture. This β value is empirically determined by occasionally analysing spike-free standard materials (e.g., DSM-3 for Mg isotope measurements) through an analysis sequence and interpolating these values across sample runs.

Critical mixtures of double spikes and samples can be obtained by iterative mixing (usually 2 or 3 iterations are needed). We prepared mixtures that deviate less than ±0.5% (molar proportion) from the critical mixture and theoretically this results in a component of inaccuracy less than 0.010‰ for δ^{26}Mg (Coath et al., 2017). Unlike most normal double-spiking procedures, Mg double spikes were added to samples after chemical purification to avoid having to repeat the purification for all iterations until a critical mixture is attained. Such spiking after chemistry requires a high-quality chemical purification process that must not fractionate Mg isotopes, but this is routinely achieved for Mg ion exchange protocols and is necessary for sample-standard bracketing procedures as well.

We report our data in delta notation against reference material DSM-3, i.e., $\delta^{26}Mg_{DSM\text{-}3}$, but in the subsequent text we abbreviate this to δ^{26}Mg. Note that we do not report both δ^{25}Mg and δ^{26}Mg as they are not obtained independently, unlike in sample-standard bracketing. Both δ^{25}Mg and δ^{26}Mg can be derived from the same value of $\alpha(\delta^{i/j}Mg) = e^{-\alpha \ln (mi/mj)} - 1$, where m_i and m_j are the masses of the two reported isotopes) and are readily inter-converted ($\delta^{25}Mg = \delta^{26}Mg/1.9569$). A check against mass-independent variation is therefore not provided by plotting δ^{25}Mg vs. δ^{26}Mg for the double-spiking data. However, using similar analysis conditions, we have demonstrated that different terrestrial standards have less than ±0.003‰ variability in a mass-independent component (Luu et al., 2019) indicating that isobaric interferences are negligible (see the supplementary material of Luu et al. (2019) for more details about the isobaric issues).

3.2. Magnesium isotope analysis

For the bulk peridotite samples from Tariat, Vitim, Zabargad and Horoman, dissolved sample solution aliquots, equivalent to about fifty micrograms of Mg, were taken from the sample digestions of Klaver et al. (2020). Powdered bulk samples from Avacha were digested with a mixture of ultra-pure concentrated HNO_3-HCl-HF (3:1:1 by volume) at 150 °C on a hotplate in closed Savillex PFA beakers. For Hawaiian xenoliths and Tibetan ophiolitic peridotites, about ten milligrams of separated mineral grains were hand-picked under a binocular, optical microscope. We only selected the freshest mineral fragments and rejected those with any signs of weathering (except for BZ-26). Selected mineral grains were first sonicated with 0.1 M HCl to remove any potential, non-visible weathering products absorbed at the mineral surface, followed by three times sonication in acetone and another three times in Milli-Q water before digestion. Then olivine, clinopyroxene and orthopyroxene grains were dissolved in cleaned, closed, 30 ml Savillex PFA beakers using a mixture of ultra-pure concentrated HNO_3-HCl-HF (3:1:1 by volume) at 150 °C on a hotplate. The solution was then dried and ultra-pure, concentrated HCl was added to digest insoluble fluorides. After complete digestion, the samples were dissolved in 1 M HNO_3 for Mg column chemistry. Spinel grains were digested with aqua regia in Carius tubes at 280 °C in an oven over two weeks. After digestion, the solution was dried and re-dissolved in 1 M HNO_3.

Separation of Mg from other matrix elements was achieved using a two-column, cation exchange chromatography procedure with Biorad AG50W-X12 resin, as described in detail in Liu et al. (2022). Briefly, 50 μg Mg in 0.2 ml 1 M HNO_3 was loaded onto a first column with 2.5 ml resin and washed with 0.5 M HF and 1 M HNO_3 to remove matrix elements. Magnesium was eluted in 2 M HNO_3. In a second column filled with 0.25 ml resin, Mg was loaded and residual matrix eluted using 0.4 M HCl before collection in 1 M HCl. Concentrated, distilled HNO_3 (15.5 M) and 30% hydrogen peroxide (Romil Ltd, SpA grade) were used to attack any potential organics after column chemistry. Yields were monitored based on 'splits' collected before and after the Mg aliquot in each column, to check there was no loss of Mg due to tailing from any drift in the elution peak relative to its calibration. The 'splits' contained negligible Mg, from which we calculate yields over 99.8% for all the samples, assuming no Mg remains adsorbed to the resin. The full procedural blank has no more than 10 ng Mg.

Magnesium isotope measurements were performed on a Thermo-Finnigan Neptune (serial no. 1020) MC-ICPMS in medium resolution mode ($M/\Delta M \geq 4000$, 5–95% peak height definition), after careful iterative addition of ^{25}Mg-^{26}Mg double spike to the samples to achieve a mixture within 0.5% of the critical value. Jet sample and H skimmer cones were used. Samples are aspirated into the mass spectrometer as a 1 μg/ml Mg sample solution in 0.3 M HNO_3 with a Savillex PFA nebuliser and Apex HF desolvating system. An intensity of about 6×10^{-10} A was obtained on ^{24}Mg (un-spiked sample), while the ^{24}Mg intensity of the 'on-peak' blank is lower than 1×10^{-13} A. An amplifier with a 10^{10} Ω feed-back resistor was used for measurements of both ^{24}Mg and ^{26}Mg beams, while an amplifier with a 10^{11}Ω feed-back resistor was used for ^{25}Mg analysis.

3.3. Uncertainties of critical mixture double spike measurements

It is important to note that we report uncertainties on δ^{26}Mg as two times the standard error of the mean (2 s.e.) of four to eight (usually six) individual runs (N in Table 1)., which in turn consist of 20 cycles with 8.4 s integration times. The 2 s.e. ascribed to samples are calculated from a standard deviation (s.d.) (2 s.e. = 2 s.d./$\sqrt{N}$, N is the number of repeated analyses) determined by a homoscedastic approach of pooling reproducibility over all the standards and samples in each analytical session. Compared to standard deviations based only on the number of repeated analyses of an individual sample, the pooled standard deviation of a session increases the dataset and the degrees of freedom and statistically gives a more reliable estimate of uncertainty (for more details on this statistical approach, see Appendix A to Steele et al., 2012).

The reproducibility of critical mixture double-spiking Mg isotope analysis was already discussed in Liu et al. (2022); the long-term reproducibility of BHVO-2 over a year in 16 analytical sessions (±0.027‰ 2 s.d.) is indistinguishable from the ±0.025‰ (2 s.e.) uncertainty we quoted for the mean of a typical 6 repeats in one analytical session (Liu et al., 2022). We argue, therefore, that there are no significant additional sources of uncertainty affecting the data over the long term and that it is reasonable to use the sample 2 s.e. from a single session as a reliable estimate of uncertainty. As an example from this study, sample S2 (a Mongolian xenolith) was measured in duplicate (repeated column chemistry, sample spiking and measurement) and yielded identical values of −0.219 ± 0.022‰ and −0.220 ± 0.030‰ (Table 1). These result contrasts with observations made for Mg isotope analyses by sample-standard bracketing, for which long-term reproducibility is typically larger than the 2 s.e. of an individual sample and often similar to the 2 s.d. of a session mean, e.g., the long-term reproducibility of DTS-2 analyses in 20 analytical sessions is ±0.06‰ (2 s.d.),

which is similar to the 2 s.d. of a typical sample mean in a single session (Teng et al., 2015a, 2015b).

Further support of the validity of our quoting 2 s.e. uncertainties is empirically demonstrated here with measurements of a set of gravimetric mixtures of a dissolution of JP-1 with the DSM-3 standard, as presented in Fig. 4 (also see Table S1). The measured Mg isotopic compositions of all the gravimetric mixtures are within measured 2 s.e. uncertainties of their calculated compositions (grey shaded region in Fig. 4).

We also analysed the reference material DSM-3 with artificially added matrix elements, to test the accuracy of the critical mixture double-spiking technique against incomplete sample purification. The matrix elements chosen are those that are least effectively removed by our chromatographic purification and mixtures are designed to represent exaggerated examples of impurities remaining after column chemistry. Our synthetic mixtures have Mg/matrix ratios which are as low as 5 whereas this value is typically >200 for our purified silicate samples (Liu et al., 2022). All mixtures of DSM-3 with matrix elements yield δ^{26}Mg within uncertainty of zero (Fig. S2b). The dataset as a whole gives an average δ^{26}Mg of 0.004 ± 0.024‰ (2 s.d., Fig. S2b). The reproducibility across this range of high matrix samples is similar to the analysis of the pure Mg solution (±0.023‰ 2 s.d., Fig. S2a) or purified samples (±0.027‰ 2 s.d., see above), which further supports the robustness of the critical mixture double-spiking technique.

3.4. δ^{26}Mg values of rock standards

A number of international rock standards have been measured during the course of this study (Table 2) in several analytical sessions. These results are within uncertainty of the data previously reported by Hin et al. (2017) using the same method. The one other study to employ critical mixture double-spiking (He et al., 2022), reports δ^{26}Mg within uncertainty for the three rock standards we have measured in common (Table 2).

Given the higher precision and more accurate mass bias normalisation by the critical mixture double-spiking approach relative to sample-standard bracketing, we do not necessarily expect perfect correspondence between our standard data and those reported in the literature (Table 2, see also discussion in He et al., 2022). For example, literature sample-standard bracketing measurements of δ^{26}Mg for BCR-2 cover a wide range of values, some overlapping with our results but with a mean that is markedly isotopically lower (Fig. 5). Nonetheless, the recommended values reported in a recent summary of geological reference material data measured by the sample-standard bracketing technique (Teng, 2017) are within uncertainty of our JP-1, BHVO-2 and DTS-2 analyses (Table 2).

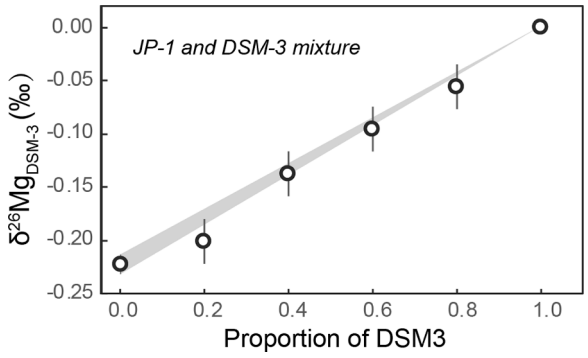

Fig. 4. Magnesium isotopic compositions of gravimetric mixtures of various proportions of reference material DSM-3 and rock standard JP-1, measured by the critical mixture double-spiking technique. The shadow triangle represents possible δ^{26}Mg compositions created by mixing of DSM3 (0‰ by definition) and JP-1 (−0.223 ± 0.010‰). All the measured mixtures are within their 2 s.e. of their respective calculated compositions.

Table 2
Magnesium isotopic compositions of geological rock standards from this study and selected literature.

	δ^{26}Mg ‰	Pooled 2 s.e.	N#	δ^{26}Mg[ref1]	δ^{26}Mg[ref2]	δ^{26}Mg[ref3]
BCR-2	−0.143	0.015	25,4 (2)		−0.126 ± 0.034	
BIR-1	−0.207	0.010	37,6 (2)	−0.194 ± 0.020		−0.27 ± 0.03
BHVO-2	−0.202	0.008	81,16 (2)	−0.186 ± 0.010	−0.188 ± 0.024	−0.24 ± 0.08
DTS-2	−0.269	0.023	10,2 (1)			−0.32 ± 0.06
JB-2	−0.120	0.013	35,5 (3)			−0.21 ± 0.02
JP-1	−0.223	0.010	53,8 (2)	−0.229 ± 0.008	−0.219 ± 0.031	−0.24 ± 0.01

[ref1] Hin et al. (2017) (critical mixture double-spiking); Note Hin et al. (2017) reported δ^{25}Mg, it is recast into δ^{26}Mg by $\delta^{26}Mg = \delta^{25}Mg \times 1.9569$.
[ref2] He et al. (2022) (critical mixture double-spiking);
[ref3] Teng (2017) (sample-standard bracketing);
The first number is the total number of repeat analyses; the number behind comma indicates the number of analytical sessions over which analyses were made and the number in brackets gives the number of separate standard digestions used.

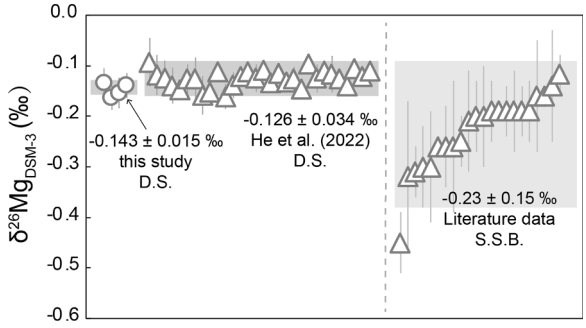

Fig. 5. Comparison of Mg isotopic compositions of rock standard BCR-2 measured by critical mixture double-spiking (D.S.), from both this study and He et al. (2022), and by sample-standard bracketing (S.S.B.) (for sources of literature S.S.B. data see He et al., 2022 and references therein).

4. Results

4.1. Magnesium isotopic fractionation among mantle minerals

δ^{26}Mg values of minerals separated from peridotites are reported in Table 3. Inter-mineral differences in Mg isotope ratios are expressed as $\Delta^{26/24}Mg_{x/y} = \delta^{26}Mg_x - \delta^{26}Mg_y$, where x and y are two mineral phases (Table 3, Fig. 6). In general, spinel, clinopyroxene and orthopyroxene are heavier in their Mg isotopic compositions than olivine (Fig. 6). Since the magnitude of equilibrium isotopic fractionation is inversely dependent on the square of absolute temperature (Bigeleisen and Mayer, 1947), we also need to quantify the equilibration temperatures of the peridotites. These have been estimated with the several thermometers (Brey and Köhler, 1990; De Hoog et al., 2010) and are close to 1000 °C for all the samples (Table 3, Fig. 3). Our empirically determined $\Delta^{26/24}Mg_{cpx/ol}$ and $\Delta^{26/24}Mg_{opx/ol}$ are consistent with a range of theoretical predictions at the corresponding temperatures (Young et al., 2009, Schauble, 2011; Huang et al., 2013), while the $\Delta^{26/24}Mg_{sp/ol}$, are all higher than corresponding theoretical calculations (Fig. 7).

4.2. Magnesium isotopic composition of mantle peridotites

Our analyses of fresh, whole rock powders of peridotite samples have a very limited δ^{26}Mg range from −0.269 ± 0.023‰ to −0.213 ±

Table 3
Mineral Mg isotopic compositions and inter-mineral Mg isotopic differences.

Sample ID	T_{BKN} (°C)*	Minerals	$\delta^{26}Mg$	2 s.e.	N	$\Delta^{26/24}Mg_{Ol/Cpx}$	2 s.e.	$\Delta^{26/24}Mg_{Ol/Opx}$	2 s.e.	$\Delta^{26/24}Mg_{Ol/Sp}$	2 s.e.
77SL405	1073 ± 55	Olivine	−0.199	0.028	6	−0.111	0.043	−0.023	0.043	−0.205	0.041
		Clinopyroxene	−0.088	0.032	6						
		Orthopyroxene	−0.176	0.032	6						
		Spinel	0.006	0.030	4						
77SL466	1035 ± 55	Olivine	−0.270	0.028	6	−0.092	0.040	−0.038	0.043	−0.275	0.041
		Clinopyroxene	−0.178	0.028	6						
		Orthopyroxene	−0.232	0.032	6						
		Spinel	0.005	0.030	4						
77SL470	976 ± 55	Olivine	−0.242	0.028	6	−0.107	0.043	−0.050	0.043	−0.245	0.041
		Clinopyroxene	−0.135	0.032	6						
		Orthopyroxene	−0.192	0.032	6						
		Spinel	0.003	0.030	4						
88PAL12	869 ± 95	Olivine	−0.257	0.028	6					−0.345	0.041
		Spinel	0.088	0.030	4						
115048–26	963 ± 55	Olivine	−0.293	0.028	6	−0.160	0.043	−0.111	0.043	−0.402	0.043
		Clinopyroxene	−0.133	0.032	6						
		Orthopyroxene	−0.182	0.032	6						
		Spinel	0.109	0.032	4						
BZ-26	914 ± 100	Olivine	−0.181	0.016	26	−0.081	0.033	−0.010	0.033		
		Clinopyroxene	−0.100	0.029	6						
		Orthopyroxene	−0.171	0.029	6						
Mean#						**−0.118**	**0.018**	**−0.056**	**0.018**		
Corrected to the average 1245 K						**−0.118**	**0.018**	**−0.056**	**0.018**		

* The temperature is calculated from the two-pyroxene thermometer, Brey and Köhler (1990), at 1.8 GPa pressure.
\# The mean of $\Delta^{26/24}Mg_{Ol/Sp}$ is not reported due to the potential kinetic isotope fractionation influence, see text for details; BZ-26 is not included.

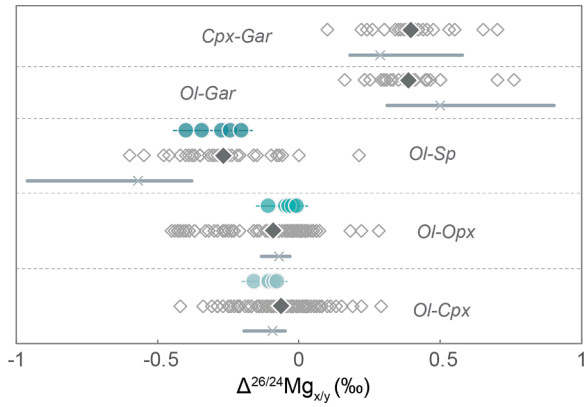

Fig. 6. Inter-mineral Mg isotopic differences. Filled green samples from this study. Open grey diamonds are individual literature data from Handler et al., 2009; Yang et al., 2009; Liu et al., 2011; Huang et al., 2011; Pogge von Strandmann et al., 2011; Xiao et al., 2013, 2016; Lai et al., 2015; Hu et al., 2016; An et al., 2017; Liu et al., 2017; Zhao et al., 2017; Chen et al., 2018; Stracke et al., 2018, Hu et al., 2020). Solid grey diamonds show average literature values for given mineral pairs. Grey lines are theoretical predictions from Schauble (2011) and Huang et al. (2013), using pressures of 0 to 2 GPa and temperatures from 1000 K to 1600 K. The cross on the grey line marks the theoretically predicted value at 1000 °C and 0 GPa, as appropriate for the equilibrium conditions recorded in the xenoliths of this study. Inter-mineral fractionations determined by sample-standard bracketing are too numerous to allow individual uncertainties to be shown but are typically over ±0.15‰.

0.038‰ (Table 1). There is no systematic covariation between bulk Mg# and $\delta^{26}Mg$ (Fig. 8a). Sample BZ-26, which has clear petrographic evidence of alteration (Fig. 2c) and the highest LOI, has anomalously high $\delta^{26}Mg$, −0.151 ± 0.022‰ (Fig. 8a).

The $\delta^{26}Mg$ of some samples were characterised by analysis of their olivines rather than whole rock powder (Table 4). Given the dominance of olivine on Mg budget of peridotites, these values very closely approximate to their bulk Mg isotopic composition (cf. Tables 1 and 4). Samples with optically fresh olivines show a limited variation in $\delta^{26}Mg$ from −0.293 ± 0.028‰ to −0.199 ± 0.028‰, while the olivines of altered BZ-26 yield the isotopically heaviest composition (−0.181 ± 0.016‰) (Fig. 8b). The bulk $\delta^{26}Mg$ for these peridotites can be calculated, which we do in two ways. For the Hawaiian xenoliths, measurements of $\delta^{26}Mg$ were made for all constituent mineral phases (Table 3), which together with modal abundances and MgO contents of these phases (Bizimis et al., 2004, 2007), allow bulk $\delta^{26}Mg$ to be calculated (Fig. 8c, Table 1). For the Tibetan samples, we only measured the Mg isotopic compositions of olivine grains, but we use the average inter-mineral isotopic differences (Table 3) in conjunction with reported modal abundances and MgO contents (Bao et al., 2013, 2014) to estimate bulk $\delta^{26}Mg$ (Table 1). Such calculations are quite insensitive to uncertainties in the inputs other than the measured olivine $\delta^{26}Mg$, which dominates overall uncertainty.

Our numerically reconstituted bulk $\delta^{26}Mg$ are plotted with bulk analyses in Fig. 8c, including the previously reported $\delta^{26}Mg$ of mantle peridotites using the same analytical method (Hin et al., 2017). The data show excellent agreement with each other. Excluding the perturbed BZ-26, all the critical double-spiking analyses of peridotite samples yield a mean $\delta^{26}Mg = -0.236 \pm 0.036$‰ (2 s.d.) (Fig. 8c).

5. Discussion

5.1. The influence of secondary alteration

Seafloor alteration increases Mg isotope ratios to values of $\delta^{26}Mg \sim -0.15$ to −0.05‰ in altered, abyssal peridotites (Liu et al., 2017). This results from loss of isotopically light Mg during hydrothermal alteration (Beinlich et al., 2014; Liu et al., 2017; Zhao et al., 2023). Even the least altered bulk abyssal peridotites analysed by Liu et al. (2017) have LOI of ~1 wt% and $\delta^{26}Mg \sim -0.15$‰, which are similar characteristics to our one, evidently altered sample, BZ-26 (LOI 1.04 wt% and bulk $\delta^{26}Mg = -0.151 \pm 0.022$‰, Fig. 8a). These prior results are therefore in keeping with BZ-26 having experienced an episode of hydrothermal alteration by seawater during exhumation, as previously proposed for some Zabargad samples (e.g., Petrini et al., 1988).

Unlike BZ-26, we could pick optically clear olivines from the fresh, low LOI samples (less than 0.5 wt%) for all Tibetan ophiolite peridotite

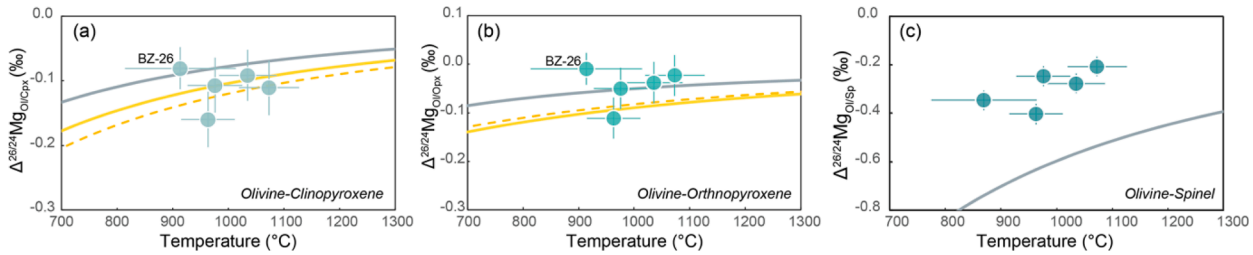

Fig. 7. Inter-mineral Mg isotopic differences for (a) olivine-clinopyroxene, (b) olivine-orthopyroxene and (c) olivine-spinel pairs plotted against two-pyroxene equilibrium temperatures for the same samples and compared to theoretical predictions at 0 GPa (Schauble, 2011, grey line), 0 GPa (Huang et al., 2013, yellow line), and 20 GPa (Huang et al., 2013, dashed yellow line). BZ-26 is highlighted.

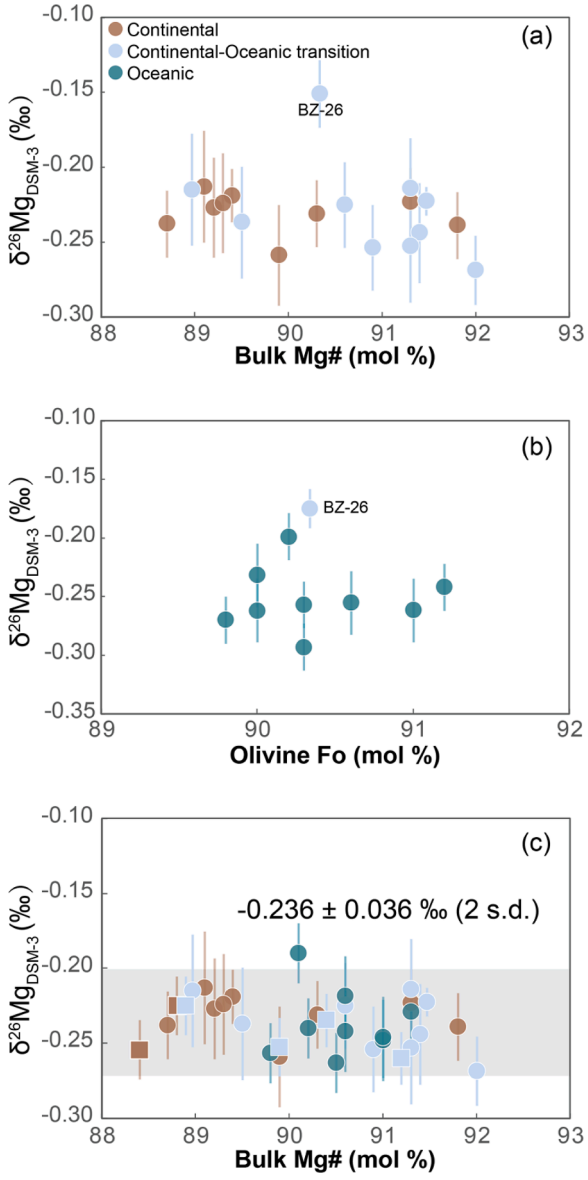

Fig. 8. Magnesium isotopic composition plotted against: (a) bulk Mg# (mol%) for powdered bulk samples from this study (b) olivine Fo content (mol%) for hand-picked olivine grains from this study, (c) bulk Mg# (mol%) of all peridotites analysed by critical mixture double-spiking, including bulk and reconstituted bulk analyses from this study (circles) together with data from Hin et al (2017) (squares). Different tectonic settings of the peridotites are indicated by different colours. The clearly altered sample (BZ26) is highlighted in (a) and (b) but excluded from (c) and the mean δ^{26}Mg (±2sd) reported in (c).

Table 4
Magnesium isotopic compositions of hand-picked olivine grains from mantle peridotites.

Sample ID	δ^{26}Mg	Pooled 2 s.e.	N
Zabargad sample			
BZ-26	−0.181	0.016	26
Hawaiian xenoliths			
77SL405	−0.199	0.028	6
77SL466	−0.270	0.028	6
77SL470	−0.242	0.028	6
88PAL12	−0.257	0.028	6
115048-26	−0.293	0.028	6
Tibetan ophiolite samples			
ZN10	−0.255	0.032	10
ZB87	−0.232	0.032	10
TB93	−0.262	0.032	10
TB157	−0.262	0.032	10

samples, which gave reconstructed bulk δ^{26}Mg within error of our fresh bulk peridotites from other localities. These results contrast with a previous study of Su et al. (2015), who reported bulk Tibetan ophiolite peridotites with an average δ^{26}Mg ~0.05‰ higher than normal mantle. Yet the bulk samples with elevated δ^{26}Mg reported by Su et al. (2015) have LOI from 3 to 14 wt% and inevitably suffered secondary alteration, which can account for their slightly high δ^{26}Mg. While elevated LOI provides a useful sign of possible perturbation of Mg isotopic compositions, but we stress that there is not a simple, universal relationship between LOI and δ^{26}Mg that would allow accurate prediction of the magnitude of such an influence in any given peridotite sample.

5.2. Inter-mineral Mg isotopic fractionation

Inter-mineral Mg isotopic fractionation has been theoretically predicted (Young et al., 2009, Schauble, 2011; Huang et al., 2013) and determined by analyses in many studies (Handler et al., 2009; Yang et al., 2009; Liu et al., 2011; Huang et al., 2011; Pogge von Strandmann et al., 2011; Xiao et al., 2013, 2016; Lai et al., 2015; Hu et al., 2016; An et al., 2017; Liu et al., 2017; Zhao et al., 2017; Chen et al., 2018; Stracke et al., 2018; Hu et al., 2020) (Fig. 6). Yet the uncertainty of sample-standard bracketing results in a limited ability to resolve the magnitude and even sense of fractionations predicted by theory, e.g., literature data yield a wide range of $\Delta^{26/24}$Mg $_{ol/cpx}$ (~−0.2 to +0.1‰) and an ever wider one for $\Delta^{26/24}$Mg $_{ol/opx}$ (~−0.25 to +0.15‰) (Fig. 6). Our high precision data refine previous empirical determinations for $\Delta^{26/24}$Mg $_{ol/cpx}$ and $\Delta^{26/24}$Mg $_{ol/opx}$ and show good agreement with theory (Fig. 7).

We correct the $\Delta^{26/24}$Mg $_{ol/cpx}$ and $\Delta^{26/24}$Mg $_{ol/opx}$ of each sample to a common temperature of 1245 K, using the well-known relationship of isotopic fractionation with $1/T^2$ (Bigeleisen and Mayer, 1947). BZ-26 gives temperature corrected values of $\Delta^{26/24}$Mg $_{ol/cpx}$ and $\Delta^{26/24}$Mg $_{ol/opx}$ that are 0.05‰ higher than average values for the Hawaiian xenoliths. This is in keeping with the difference in δ^{26}Mg between the picked, but still altered olivines from this sample (Fig. 2c) and the mean value for olivines in fresh peridotites (Fig. 8b and Table 4), assuming

pyroxenes are more robust to aqueous alteration and minimally perturbed. We therefore exclude BZ26 in calculating mean $\Delta^{26/24}Mg_{ol/cpx}$ of −0.118 ± 0.018‰ and $\Delta^{26/24}Mg_{ol/opx}$ of −0.056 ± 0.018‰, at 1245 K (Table 3).

In comparison to the olivine-pyroxene fractionations, our new $\Delta^{26/24}Mg_{ol/sp}$ show a wide range in values compared to their uncertainties. Moreover, they are all higher than theoretical values at appropriate temperatures (Fig. 7c). Variable chemical composition (e.g., Cr and Fe content) can influence Mg isotope partitioning into spinel (Liu et al., 2011; Schauble, 2011; Huang et al., 2013; Stracke et al, 2018), but the $\Delta^{26/24}Mg_{ol/sp}$ show no systematic variation with either Cr# or spinel FeO content (Fig. 9). Instead, we suggest that there may be a kinetic control on the measured $\Delta^{26/24}Mg_{ol/sp}$ caused by incomplete diffusive re-equilibration of Fe-Mg between spinel and olivine during post-eruptive, xenolith cooling. Kinetic, Mg isotopic fractionation has previously been inferred for slowly cooled xenoliths (Pogge von Strandmann et al., 2011).

Fe-Mg exchange between olivine and spinel can continue to a relatively low temperature of ~650 °C (Fabriès, 1979; Henry and Medaris, 1980). A more recent study has shown that temperatures estimated from Fe-Mg exchange olivine-spinel thermometry are generally ~200 °C lower than estimates from other thermometers due to late-stage Fe-Mg exchange (Ramsey et al., 2021). Such re-equilibration generally occurs by Mg diffusing from olivine to spinel (Roeder et al., 1979; Lehmann, 1983), and if incomplete, should lower the $\delta^{26}Mg$ of the spinel due to the addition of faster moving, lighter Mg isotopes. This would result in a higher $\Delta^{26/24}Mg_{ol/sp}$. Relative to the major silicate phases, the small spinel grains have larger surface area to volume and lower Mg contents, as well as a higher diffusivity of Mg (Liermann and Ganguly, 2002; Dohmen and Chakraborty, 2007), which should result in more marked perturbation of spinel by a late-stage diffusive flux of Mg (Ozawa, 1983). Hence these kinetic effects are only evident in $\Delta^{26/24}Mg_{ol/sp}$ (Fig. 7). More work is required to substantiate this rationalisation but in keeping with these inferences we use only the lowest $\Delta^{26/24}Mg_{ol/sp}$ (−0.402‰) in subsequent calculations.

5.3. Homogeneity of fresh mantle peridotites

A striking aspect of our analyses of peridotites is their homogeneity in $\delta^{26}Mg$. The samples examined show a wide range in geochemical characteristics that largely reflect variable amounts of melt depletion and metasomatic enrichment (Fig. 1a and b). Yet there are no systematic co-variations between chemical indices of these processes and $\delta^{26}Mg$ (Fig. 10a and b). Moreover, the variability on our global mean of $\delta^{26}Mg$ = −0.236 ± 0.036‰ (2 s.d.) is close to the reproducibility of individual analyses (±0.027‰, Section 3.3). This implies that natural variability in mantle $\delta^{26}Mg$ little exceeds the uncertainty of our analyses.

Likewise, there is no relationship between peridotite $\delta^{26}Mg$ and the tectonic settings from which they derived (Figs. 8 and 10). There has been some debate as to whether or not subduction zone processes can influence the Mg isotopic composition of the mantle wedge (e.g., Teng, 2017; Hu et al., 2020; Liu et al., 2022). In this context, our remeasurements of two Avacha peridotites is significant, as these are samples of a mantle wedge (Ionov and Seitz, 2008; Ionov, 2010; Ionov et al., 2011; Bénard et al., 2017). Our new Avacha analyses have Mg isotopic compositions within error of our other mantle samples (Fig. 8c, Table 1). This contrasts with slightly elevated values previously reported for sample-standard bracketed measurements of these same mantle wedge samples (Pogge von Strandmann et al., 2011), i.e., $\delta^{26}Mg$ = −0.10 ± 0.06‰ (2 s.d.) for Av6 compared to $\delta^{26}Mg$ = −0.254 ± 0.029‰ (2 s.e.) reported here (Table 1). We therefore agree with Hu et al. (2020) who found no evidence for elevated $\delta^{26}Mg$ in these subduction related samples and obtained $\delta^{26}Mg$ = −0.26 ± 0.04‰ (2 s.d.) for Av6 specifically. The mean $\delta^{26}Mg$ = −0.21 ± 0.07‰ of normal mantle peridotites presented by Pogge von Strandmann et al. (2011) is consistent with our

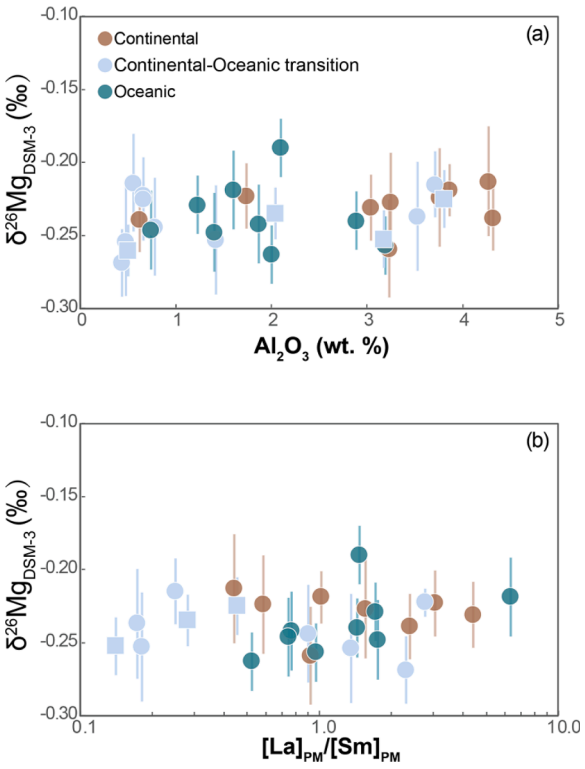

Fig. 10. (a) $\delta^{26}Mg$ of bulk peridotite samples from this study (circles) and Hin et al. (2017) (squares) plotted against a) Al_2O_3 (wt.%) and (b) primitive mantle normalised (Palme and O'Neill, 2014) La/Sm ratios. The samples are coloured according to tectonic setting.

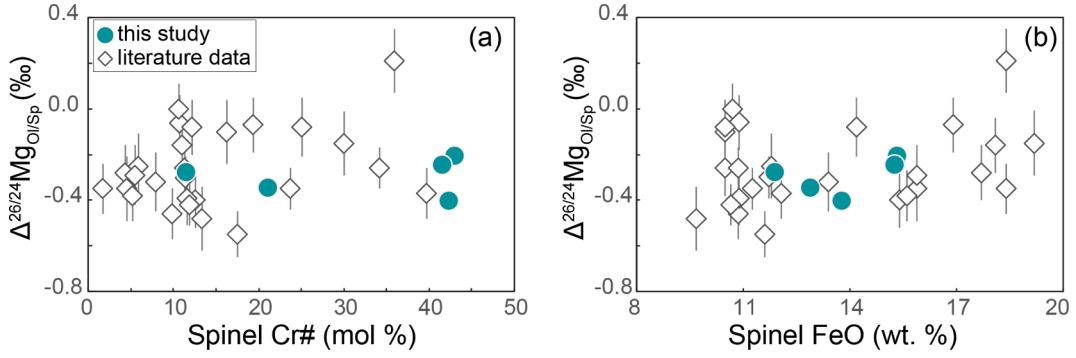

Fig. 9. Mg isotopic differences between olivine and spinel plotted against (a) spinel Cr# (mol%) and (b) spinel FeO content. Note the error bars of data from this study are too small to be visible. For references to literature data see the caption of Fig. 6.

value from critical mixture double-spiking measurements. This situation usefully illustrates that on average, sample-standard bracketing is reliable but non-systematic sources of uncertainty makes the reliability of individual samples hard to gauge.

5.4. Mg isotopic compositions of Hawaii xenolith samples and the deep mantle

Hawaiian peridotite xenolith samples have striking Hf and Os isotope ratios (e.g., Fig. 11a, Bizimis et al., 2004, 2007), which are argued to reflect variable depletion and subsequent aging, during deep-recycling of oceanic lithospheric mantle (Bizimis et al., 2007). Our analyses show no systematic variability of δ^{26}Mg with ancient depletion as proxied by ^{176}Hf/^{177}Hf (Fig. 11b). This observation reinforces the conclusion above that melt depletion does not significantly fractionate the Mg isotope ratios of mantle melt residues. In this respect, the Mg isotope system differs to some other major elements, presumably owing to the strong compatibility of Mg. Notably, Williams and Bizimis (2014) reported Fe isotopic compositions of a similar set of Hawaiian xenolith samples, that showed systematic covariations between δ^{57}Fe and Hf isotope ratios. While their reported sense of co-variation is in keeping with a predicted decrease in δ^{57}Fe with melt depletion, Williams and Bizimis (2014) were unable to quantify the magnitude of decrease in δ^{57}Fe as a function of degree of melt depletion. This indicates additional complexity in understanding δ^{57}Fe variability in the mantle.

Importantly, the Hawaiian Salt Lake Crater (SLC) xenolith samples have been argued to represent a direct sample of a mantle plume source containing deep recycled materials (Bizimis et al., 2007). There are speculations that the lowermost mantle may have distinct major element isotopic compositions as the result of primordial magma ocean solidification (e.g., Huang et al., 2014; Wu et al., 2015; Williams et al., 2021). Theoretical calculations show that highly co-ordinated Mg in the dominant lower mantle phase bridgmanite is isotopically lighter than a co-existing, fictive melt at 25GPa, 2000 K (Wu et al., 2015). Thus, cumulate bridgmanite that crystallised from a basal melt layer, could have a distinct Mg isotopic composition from upper mantle peridotite samples. Yet, all the Hawaii SLC xenolith samples have similar δ^{26}Mg to upper mantle peridotite samples (Fig. 8b and c, Tables 1 and 4).

5.5. Comparison with the literature database

We have also re-examined literature data to assess δ^{26}Mg homogeneity of mantle peridotites across a larger number of analyses. First, we filtered the literature samples to exclude pyroxenite samples and further rejected peridotites with LOI > 1 wt% (see Section 5.1), where LOI data are available. There are δ^{26}Mg values reported in the literature for 263 ultramafic, mantle-derived samples. After applying our selection criteria, 199 samples remain (Fig. 12a). A similar selection was also made of literature Mg isotope data of peridotitic olivine grains. Again, we only compiled peridotitic olivine grains from low LOI samples (less than 1 wt% for the bulk sample). We also rejected olivines from samples with low bulk LOI, but which had reported secondary alteration, i.e., serpentinization (Zhao et al., 2023). After removal of 121 samples based on these criteria, there are 87 literature values of δ^{26}Mg for peridotitic olivine grains to compare with our new data (Fig. 12b).

As is shown in Fig. 12, the literature data, both for the bulk peridotite samples and peridotitic olivine grains, have reassuringly similar means to our critical mixture double-spiking data but show more variability, at least in part reflecting greater analytical uncertainty (see Section 3.3). Bulk peridotite samples have a mean δ^{26}Mg of −0.236 ± 0.036‰ (2 s.d.) for the critical mixture double-spiking data, compared to −0.238 ± 0.107‰ (2 s.d.) for the sample-standard bracketed data. The mean δ^{26}Mg of our peridotitic olivine data is −0.252 ± 0.053‰ (2 s.d.), compared with sample-standard bracketed data of −0.256 ± 0.126‰ (2 s.d.). Although less precise, across the large, mantle dataset, the mean δ^{26}Mg obtained by sample standard bracketing is accurate (see also Hin et al., 2017).

Furthermore, since our 33 double-spiked Mg isotope data are normally distributed, passing the Shapiro-Wilk test ($p = 0.572$ for $\alpha = 0.05$), we can treat the peridotite samples as a single population and obtain a mean value of accessible mantle with 95% significance level of −0.236 ± 0.006‰ (2 s.e.). Overall, these data imply a homogeneous Mg isotopic composition of the mantle. We re-emphasise that this value is non-chondritic (mean chondritic δ^{26}Mg = −0.274 ± 0.012‰, 2 s.e., Hin et al., 2017), which Hin et al. (2017) argued to be the consequence of ~40% evaporative mass loss from the planetesimals that accreted to form the Earth. Such substantial thermal processing of terrestrial building blocks is critical for the shaping the bulk composition of the Earth for all but the most refractory elements. For example, the model presented by Hin et al. (2017) to account for the Earth's super-chondritic δ^{26}Mg also consistently explains the enigmatic elevated Mg/Si of the mantle. It further implies that more volatile elements, such as the alkalis, must be delivered by bodies with a radically different thermal histories, likely from a different part of the solar system, compared to those that accreted to form the more refractory bulk of the planet.

Further applying the high precision double spike technique to meteoritic samples of other rocky bodies, would equally be valuable in assessing potential evaporative losses during their accretional histories. Hin et al. (2017) made some high precision δ^{26}Mg measurements of HED and an angrite sample. However, further analyses and a careful assessment of potential magmatic fractionations, such as explored here, is critical in attempting to robustly reconstruct bulk parent body Mg isotopic compositions.

Alternatively, the super-chondritic δ^{26}Mg of the accessible mantle might be argued to result from a deep, hidden reservoir of isotopically light, cumulate bridgmanite. As documented above, however, material from the Hawaiian plume, which is plausibly linked with a source at the base of the mantle, has δ^{26}Mg within error of upper mantle samples.

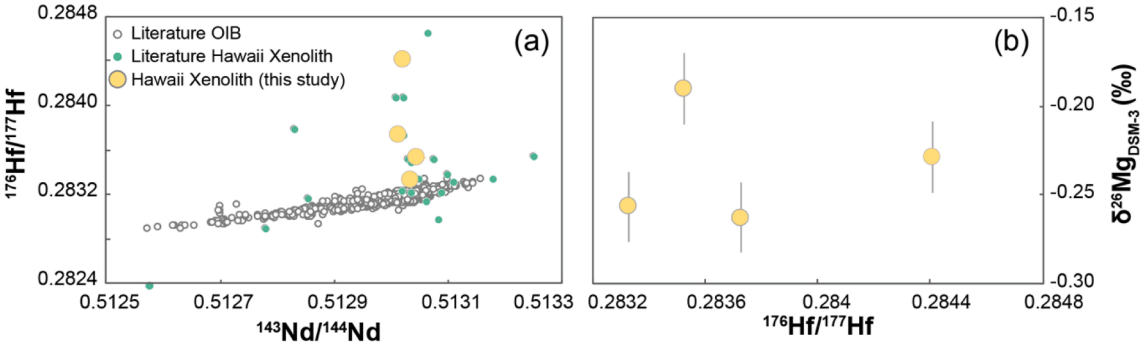

Fig. 11. (a) Radiogenic Hf isotopic compositions of Hawaiian xenoliths (green dots) reported in Bizimis et al. (2004, 2007), illustrated relative to a compilation of oceanic basalts from the literature. Samples analysed in this study shown as larger yellow circles. (b) Mg isotopic composition of Hawaii xenoliths plotted against ^{176}Hf/^{177}Hf.

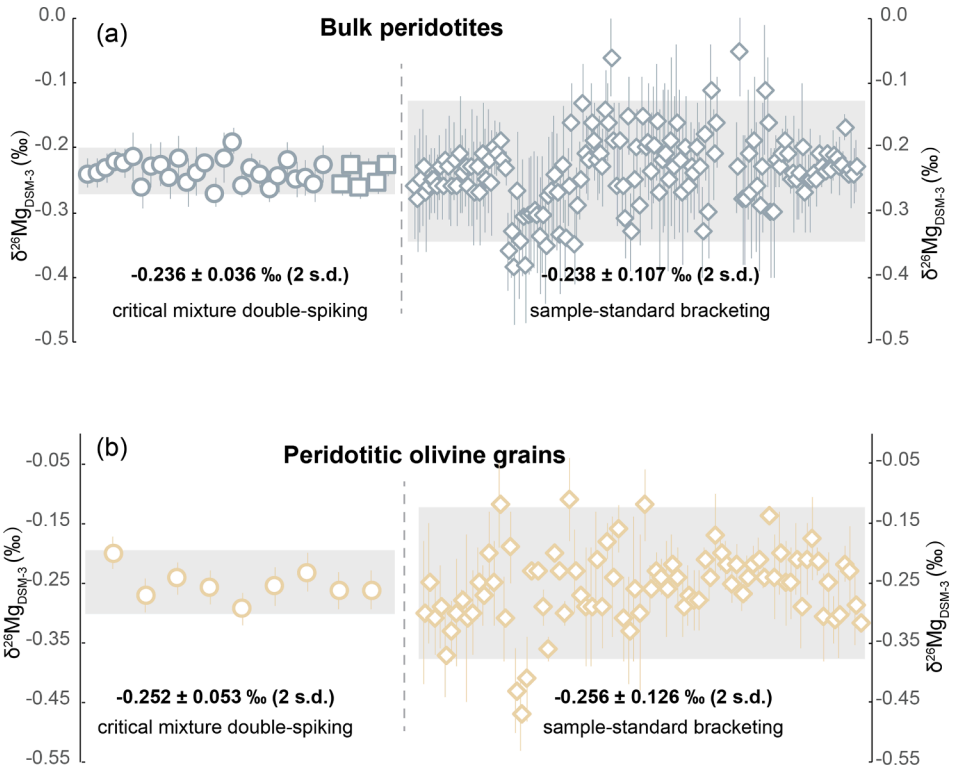

Fig. 12. Comparison of Mg isotopic compositions measured by critical mixture double spiking and sample standard bracketing of (a) bulk peridotites and (b) peridotitic olivine. Sample-standard bracketing literature data are from Handler et al., 2009; Yang et al., 2009; Bourdon et al., 2010; Teng et al., 2010; Huang et al., 2011; Liu et al., 2011; Pogge von Strandmann et al., 2011; Xiao et al., 2013, 2016; Lai et al., 2015; Su et al., 2015; Wang et al., 2016; An et al., 2017; Stracke et al., 2018; Hu et al., 2020. Data from Hin et al. (2017), are included as squares in the critical mixture double-spiking data. All samples with bulk LOI > 1 wt% are excluded from these compilations.

5.6. Modelling of Mg isotope fractionation during partial melting

It has been argued that there are no detectable Mg isotopic differences between melts and their sources during partial melting (Teng et al., 2010). More recent modelling (Zhong et al., 2017; Stracke et al., 2018; Wang et al., 2020; Soderman et al., 2022) suggest that a primitive melt could have a fractionated Mg isotope ratio relative to its source, especially considering lithologically heterogeneous mantle sources containing pyroxenite. However, these studies make contrasting predictions, dependent on their different adopted estimates of the melt-solid fractionation factor, which was unknown at the time of their publication. Zhong et al. (2017) argued that melts from both garnet pyroxenite and garnet peridotite could be 0.1‰ lower in δ^{26}Mg than their initial sources, while Wang et al. (2020) suggested melts from garnet pyroxenite can be up to ~0.1‰ higher in δ^{26}Mg. Yet Stracke et al. (2018) argued the melts from both garnet pyroxenite and garnet peridotite have δ^{26}Mg only ~0.03‰ lighter than their initial sources. Finally, Soderman et al. (2022) showed that melts from peridotites are almost indistinguishable from their sources in their Mg isotopic compositions (less than 0.02‰ difference) and partial melts from garnet pyroxenites could have Mg isotope compositions up to ~0.1‰ heavier.

Here, we combine our new inter-mineral isotopic differences with a determination of equilibrium olivine-melt fractionation from our previous study (Liu et al., 2022), $\Delta^{26}Mg_{ol\text{-}melt} = -0.071 \pm 0.01$‰ (at 1438 K), to model Mg isotope fractionation during partial melting. The fractionation factors between olivine, clinopyroxene and orthopyroxene are taken from our inter-mineral fractionation measurements summarised in Table 3. The fractionation factors between garnet-olivine and garnet-clinopyroxene are taken from the mean values of literature data (Fig. 6). The bulk solid-melt fractionation factors are calculated through the weighted average of individual mineral-melt fractionation factors, themselves calculated by combination of the olivine-melt and mineral–mineral fractionation factors (Table S2). Calculations are based on a non-modal, incremental batch melting model (Shaw, 2006) and the Mg isotopic compositions of each melt increment are determined based on mass-balance. Three lithologies, spinel peridotite, garnet peridotite and garnet pyroxenite, are considered by applying the experimentally constrained melting reactions (Robinson et al., 1998; Walter, 1998; Petermann and Hirschmann, 2003). The inputs to the partial melting model, the instantaneous melt-residue Mg isotope difference and the derivation of the formulae are presented in the supplementary material. The results are illustrated in Fig. 13.

The δ^{26}Mg of the residual solid, from fertile Mg# of 89.7 to depleted Mg# of 91.7, no matter what initial lithology, varies by less than 0.002‰. Over this range of melt depletion, there is less than 7% fractional loss of Mg from the solid, due to the compatible nature of Mg and this explains why δ^{26}Mg the strongly buffered. This model result is consistent with our observations that peridotite samples, with Mg# varying from 88.7 to 92.0 and coupled variations in Al_2O_3 contents from 4.32 to 0.44 wt%, have indistinguishable Mg isotopic compositions (Figs. 8c and 10a). Yet, the δ^{26}Mg in melts from all three sources deviate from their source values by different magnitudes: the δ^{26}Mg of melts from spinel and garnet peridotite are elevated by 0.045 ± 0.015‰ and 0.075 ± 0.035‰, respectively. For garnet pyroxenite melting, with garnet as the residual mineral, the melts have δ^{26}Mg ~ 0.123 ± 0.050‰ higher than their sources. The differences in the results between our calculations and previous modelling (Zhong et al., 2017; Stracke et al., 2018; Soderman et al., 2022) is due to the different values used for the solid-melt fractionation factor.

Yet, the modelling results are not seemingly mirrored in measured Mg isotope data of mantle derived melts. Sample-standard bracketing literature data of MORB and OIB sample have similar Mg isotopic compositions that scatter around peridotite values without any systematic bias to heavier values (Fig. 14). Although most of the values plotted in Fig. 13 are sample-standard bracketing data, as shown in the last section, the average values of this approach typically appear accurate (Fig. 12). Moreover, Fig. 14 also includes a smaller collection of critical mixture double-spiking analyses of mantle derived samples which are not clearly heavier than mantle peridotite values. As shown by Liu et al (2022), initial magmatic fractionation of olivine should lead to evolved melts becoming heavier in their Mg isotopic compositions, so the non-primitive nature of magmas analysed does not provide an

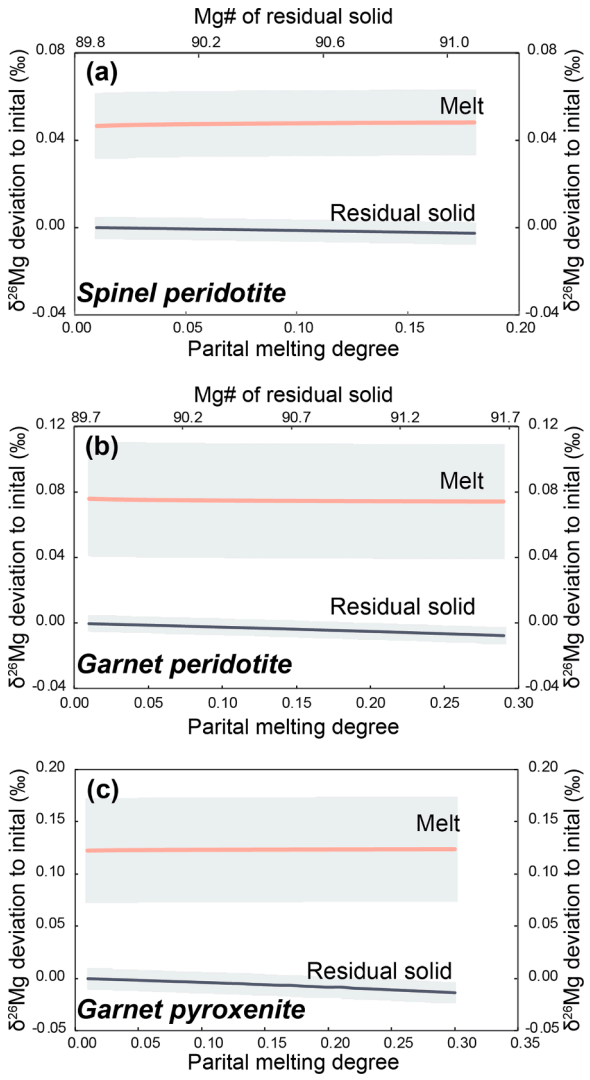

Fig. 13. Calculations of Mg isotopic fractionation relative to initial mantle composition during partial melting of three lithologies (a) spinel peridotite, (b) garnet peridotite and (c) garnet pyroxenite. The shadow bar indicates the 2 s.d. uncertainty, estimated from the uncertainties of solid–solid, and solid-melt Mg isotope fractionation factors.

explanation of their unexpectedly low δ^{26}Mg.

Therefore, additional processes to equilibrium isotopic fractionation between melt and major mafic phases must be involved in accounting for the Mg isotope compositions of basaltic melts. A plausible explanation is diffusive fractionation during melt-solid interaction. Several studies (e.g., Zhao et al., 2012; Xiao et al., 2013) have argued that anomalously large Mg and Fe isotopic differences between co-existing mineral phases in some xenoliths indicate kinetic fractionations between melt and solid. These unusual samples presumably reflect a large melt to rock ratio in order for the residual solid composition to have been sufficiently perturbed. However, the dominance of peridotite in the Mg mass balance between melt and mantle at lower melt-rock ratios can result in a notable change in the δ^{26}Mg of melt during diffusional exchange with a peridotite whose δ^{26}Mg is imperceptibly affected (Fig. 15). We suggest that this latter scenario might be common and can help account for the values and variability of δ^{26}Mg in mantle derived melts.

Commonly accepted concepts of melt production offer a rationalisation for diffusional exchange between melt and solid during this process. Melting by adiabatic decompression leads to melting over a range of depths and degrees of melt depletion of the residual solid.

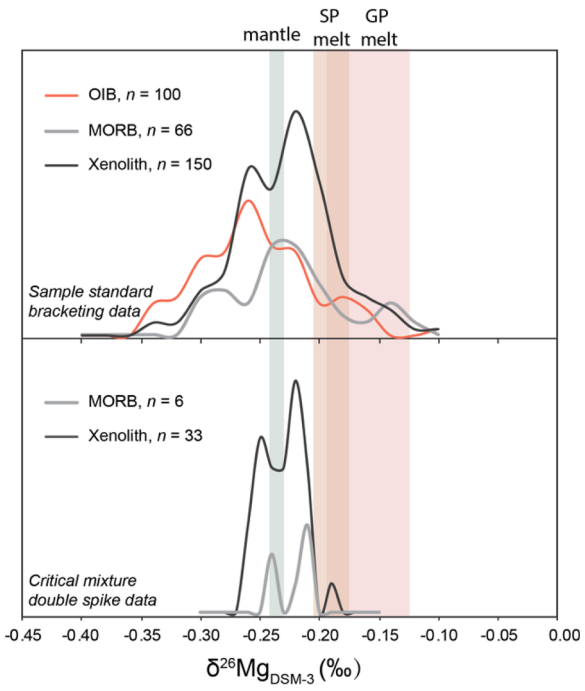

Fig. 14. Comparison of Mg isotopic compositions of mantle xenoliths and mantle derived melts (MORB and OIB). (a) Sample-standard bracketing data are from Handler et al., 2009; Yang et al., 2009; Bourdon et al., 2010; Teng et al., 2010; Huang et al., 2011; Liu et al., 2011; Pogge von Strandmann et al., 2011; Xiao et al., 2013, 2016; Lai et al., 2015; Wang et al., 2016; An et al., 2017; Zhong et al., 2017; Stracke et al., 2018; Hu et al., 2020. (b) Critical mixture double-spiking data are from Hin et al. (2017), Liu et al. (2022) and this study. The shadow bars indicate the δ^{26}Mg range of mantle and predicted mantle derived melt compositions: mantle, −0.236 ± 0.006‰; SP melt (spinel peridotite melt), −0.190 ± 0.015‰; GP melt (garnet peridotite melt), −0.160 ± 0.035‰ (see Fig. 13).

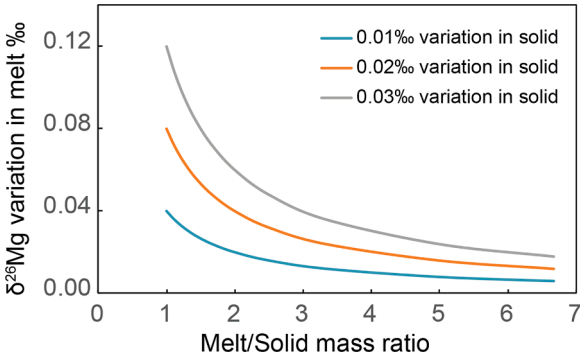

Fig. 15. The illustration of tiny Mg isotope variation in the solid would lead to significant Mg isotope variation in melt, depends on the variable melt/solid mass ratio. Assuming a closed system and thus, following mass conservative law. Note the solid here only indicates the part which interacted with the melt.

Initial, deep melts that are relatively Fe rich with low Mg/Fe and residual solids at the top of the melting column have high Mg/Fe. Several lines of argument suggest typical decompression melting of the mantle is fractional (e.g., Klein and Langmuir 1987; Johnson et al., 1990) such that melts travel in disequilibrium to the surface. Thus, at the top of the melting column, melts will be out of Mg/Fe equilibrium with the solid residue. The melts have too low Mg/Fe to be in equilibrium with the peridotites. They will attempt to equilibrate with the surrounding mantle by exchanging Fe with Mg. In this case the mantle will be enriched in faster diffusing light isotopes of Fe from the melt and

depleted in light Mg isotopes during diffusing Mg to the melt. Several studies have demonstrated Mg-Fe isotopic fractionation can be generated in olivines, emphasising that the diffusivities of Mg and Fe are sufficiently fast for this to occur on the timescales of magmatic processes (Dauphas et al., 2010; Teng et al., 2011; Sio et al., 2013; Oeser et al., 2015).

This thought experiment therefore predicts that melts which have partially equilibrated at the top of their melting columns should have isotopically lighter Mg and heavier Fe than predicted by simple equilibrium fractionation. As noted already, mantle derived melts with Mg isotopic compositions that are lighter than predicted are widely observed (Fig. 14). Moreover, the empirically determined Fe isotope composition of the oceanic basalt samples are heavier than the theoretical partial melting modelling predictions (e.g., Dauphas et al., 2014). Thus, the complementary departures of Mg and Fe isotope ratios of mantle derived melts from values expected from equilibrium melting are consistent with partial Mg-Fe exchange with residual peridotite en route to the surface. Currently this is a general observation for a global dataset, but a better test would be to obtain high precision analyses on both systems on the same set of samples.

If this kinetic isotope fractionation hypothesis is true, it undermines the utility of Mg and Fe isotope compositions to trace the mantle heterogeneity since subtle equilibrium isotopic fractionations can be significantly perturbed by diffusion, that depends on the rate of processes during melt migration to the surface. These measurements may provide useful information on the timescales of melt transport processes, but this is a very different paradigm to the one that currently frames interpretations of Mg and Fe isotope measurements in mantle derived melts. It is clearly of importance to investigate in more detail the role of diffusive fractionation in shaping Mg isotopic compositions of melts.

6. Conclusions

Applying the critical mixture double-spiking method, we report a dataset of high precision Mg isotope measurements of mantle peridotite samples. These samples have indistinguishable δ^{26}Mg values of −0.236 ± 0.036‰ (2 s.d.), which yield a mean δ^{26}Mg of the accessible mantle with 95% significance level of −0.236 ± 0.006‰ (2 s.e.), including the data from Hin et al. (2017). We also report Mg isotopic differences between major mantle minerals, −0.110 ± 0.018‰ for $\Delta^{26/24}Mg_{ol/cpx}$, and −0.046 ± 0.018‰ for $\Delta^{26/24}Mg_{ol/opx}$, which show good agreement with theoretical predictions at corresponding temperatures (~1000 °C). $\Delta^{26/24}Mg_{ol/sp}$ (from −0.205‰ to −0.402‰) is slightly higher than *ab initio* calculations, probably due to kinetic effects from Fe-Mg exchange between olivine and spinel during post-eruptive cooling. Using our new data we calculate Mg isotope fractionation during partial melting, and we find that partial melting has negligible influence on the residual peridotite δ^{26}Mg value (less than 0.002‰). Melting models also predict that mantle derived melts can have elevated Mg isotopic compositions (~0.04‰ to ~0.07‰ for peridotite melts and ~0.12‰ for pyroxenite melts), but current analyses of natural basalt samples do not yield such anticipated, elevated δ^{26}Mg values. We suggest that diffusive fractionation during partial Mg-Fe exchange between melt and solid during melt migration to the surface can explain that mantle derived melts have lower δ^{26}Mg than predicted by equilibrium fractionation during melting. This hypothesis has important implications for the interpretation of the Mg isotopic compositions of mantle derived melts.

Declaration of Competing Interest

The authors declare that they have no known competing financial interests or personal relationships that could have appeared to influence the work reported in this paper.

Acknowledgements

Ian Parkinson is thanked for the help of spinel digestion with Carius tube. Constructive comments from Andrea Stracke, two anonymous reviewers and associate editor Tomas Magna were of great help when improving this manuscript. This work was funded by ERC Adv Grant 883351 NONUNE building on work from NERC grant NE/LOO7428/1. Xiao-Ning Liu is financially supported by a CSC-UOB joint scholarship (China Scholarship Council – University of Bristol). M. Bizimis acknowledges funding from the NSF-OCE 1624315 grant.

Appendix A. Supplementary material

The Supplementary Material contains: Section 1, the detailed protocols of performing critical mixture double-spiking Mg isotope analysis, Section 2, formulae and their derivation for calculation of Mg isotopic fractionation during partial melting, Table S1 analyses of DSM-3—JP-1 mixtures, Table S2 summary of input data for modelling of Mg isotopic fractionation during partial melting, Table S3, the analyses of the pure DSM-3 and the DSM-3 with doped matrix elements, Fig. S1 analyses of the pure DSM-3 and DSM-3 with artificially added matrix elements, Fig. S2 calculated melt-residue Mg isotope differences for the melting model. Supplementary material to this article can be found online at https://doi.org/10.1016/j.gca.2023.08.011.

References

Albarède, F., Beard, B., 2004. Analytical methods for non-traditional isotopes. Rev. Mineral. Geochem. 55, 113–152.
An, Y., Huang, J.-X., Griffin, W.L., Liu, C., Huang, F., 2017. Isotopic composition of Mg and Fe in garnet peridotites from the Kaapvaal and Siberian cratons. Geochim. Cosmochim. Acta 200, 167–185.
Bao, P.-S., Su, L., Wang, J., Zhai, Q.-G., 2013. Study on the tectonic setting for the ophiolites in Xigaze, Tibet. Acta Geol. Sin. (English Ed.) 87, 395–425.
Bao, P.-S., Su, L., Wang, J., Zhai, Q.-G., 2014. Origin of the Zedang and Luobusa ophiolites, Tibet. Acta Geol. Sin. (English Ed.) 88, 669–698.
Beinlich, A., Mavromatis, V., Austrheim, H., Oelkers, E.H., 2014. Inter-mineral Mg isotope fractionation during hydrothermal ultramafic rock alteration–Implications for the global Mg-cycle. Earth Planet. Sci. Lett. 392, 166–176.
Bénard, A., Arculus, R.J., Nebel, O., Ionov, D.A., McAlpine, S.R.B., 2017. Silica-enriched mantle sources of subalkaline picrite-boninite-andesite island arc magmas. Geochim. Cosmochim. Acta 199, 287–303.
Bigeleisen, J., Mayer, M.G., 1947. Calculation of equilibrium constants for isotopic exchange reactions. J. Chem. Phys. 15, 261–267.
Bizimis, M., Sen, G., Salters, V., 2004. Hf-Nd isotope decoupling in the oceanic lithosphere: constrains from spinel peridotite from Oahu, Hawaii. Earth Planet. Sci. Lett. 217, 43–58.
Bizimis, M., Griselin, M., Lassiter, J.C., Salter, V., Sen, G., 2007. Ancient recycled mantle lithosphere in the Hawaiian plume: Osmium-Hafnium isotopic evidence from peridotite mantle xenoliths. Earth Planet. Sci. Lett. 257, 259–273.
Bourdon, B., Tipper, E.T., Fitoussi, C., Stracke, A., 2010. Chondritic Mg isotope composition of the Earth. Geochim. Cosmochim. Acta 74, 5069–5083.
Brey, G.P., Köhler, T., 1990. Geothermobarometry in four-phase lherzolites II. New thermobarometers, and practical assessment of existing thermobarometers. J. Petrol. 31, 1353–1378.
Brooker, R., James, R., Blundy, J., 2004. Trace elements and Li isotope systematics in Zabargad peridotites: evidence of ancient subduction processes in the Red Sea mantle. Chem. Geol. 212, 179–204.
Brueckner, H.K., Elhaddad, M.A., Hamelin, B., Hemming, S., Kröner, A., Reisberg, L., Seyler, M., 1995. A Pan African origin and uplift for the gneisses and peridotites of Zabargad island, Red Sea: A Nd, Sr, Pb, and Os isotope study. J. Geophys. Res.: Solid Earth 100, 22283–22297.
Carlson, R.W., Ionov, D.A., 2019. Compositional characteristics of the MORB mantle and bulk silicate earth based on spinel peridotites from the Tariat Region, Mongolia. *Geochim. Cosmochim. Acta* 257, 206–223.
Chen, L.-M., Teng, F.-Z., Song, X.-Y., Hu, R.-Z., Yu, S.-Y., Zhu, D., Kang, J., 2018. Magnesium isotopic evidence for chemical disequilibrium among cumulus minerals in layered mafic intrusion. Earth Planet. Sci. Lett. 487, 74–83.
Coath, C.D., Elliott, T., Hin, R.C., 2017. Double-spike inversion for three-isotope systems. Chem. Geol. 451, 78–89.
Dauphas, N., Roskosz, M., Alp, E.E., Neuville, D.R., Hu, M.Y., Sio, C.K., Tissot, F.L.H., Zhao, J., Tissandier, L., Médard, E., Cordier, C., 2014. Magma redox and structural controls on iron isotope variations in Earth's mantle and crust. Earth Planet. Sci. Lett. 398, 127–140.
Dauphas, N., Teng, F.-Z., Arndt, N.T., 2010. Magnesium and iron isotopes in 2.7 Ga Alexo komatiites: Mantle signature, no evidence for Soret diffusion, and identification of diffusive transport in zoned olivine. Geochim. Cosmochim. Acta 74, 3274–3291.

De Hoog, J.C., Gall, L., Cornell, D.H., 2010. Trace-element geochemistry of mantle olivine and application to mantle petrogenesis and geothermobarometry. Chem. Geol. 270, 196–215.
Dodson, M.H., 1963. A theoretical study of the use of internal standards for precise isotopic analysis by the surface ionization technique: Part I — General first-order algebraic solutions. J. Sci. Instrum. 40, 289–295.
Dohmen, R., Chakraborty, S., 2007. Fe-Mg diffusion in olivine II: Point defect chemistry, change of diffusion mechanisms and a model for calculation of diffusion coefficients in natural olivine. Phys. Chem. Miner. 34, 597–598.
Dupuy, C., Mével, C., Bodinier, J.L., Savoyant, L., 1991. Zabargad peridotite: evidence for multistage metasomatism during Red Sea rifting. Geology 19, 722–725.
Fabriès, J., 1979. Spinel-olivine geothermometry in peridotites from ultramafic complexes. Contrib. Miner. Petrol. 69, 329–336.
Galy, A., Yoffe, O., Janney, P.E., Williams, R.W., Cloquet, C., Alard, O., Halicz, L., Wadwha, M., Hutcheon, I.D., Ramon, E., Carignan, J., 2003. Magnesium isotopes heterogeneity of the isotopic standard SRM980 and new reference materials for magnesium-isotope-ratio measurements. J. Anal. At. Spectrom 18, 1352–1356.
Handler, M.R., Baker, J.A., Schiller, M., Bennett, V.C., Yaxley, G.M., 2009. Magnesium stable isotope composition of Earth's upper mantle. Earth Planet. Sci. Lett. 282, 306–313.
He, Y.-S., Sun, A.-Y., Zhang, Y.-C., Yang, R.-Y., Ke, S., Wang, Y., Teng, F.-Z., 2022. High-precision and high accuracy magnesium isotope analysis on multiple-collector inductively coupled plasma mass spectrometry using a critical mixture double spike technique. Solid Earth Sci. 7, 188–199.
Hébert, R., Bezard, R., Guilmette, C., Dostal, J., Wang, C.-S., Liu, Z.-F., 2012. The Indus–Yarlung Zangbo ophiolites from Nanga Parbat to Namche Barwa syntaxes, south- ern Tibet: first synthesis of petrology, geochemistry, and geochronology with incidences on geodynamic reconstructions of Neo-Tethys. Gondw. Res. 22, 377–397.
Henry, D.J., Medaris, L.G., 1980. Application of pyroxene and olivine-spinel geothermometers to spinel peridotites in southwestern Oregon. Am. J. Sci. 280, 211–231.
Hin, R.C., Coath, C.D., Carter, P.J., Nimmo, F., Lai, Y.-J., Pogge von Strandmann, P.A.E., Willbold, M., Leinhardt, Z.M., Walter, M.J., Elliott, T., 2017. Magnesium isotope evidence that accretional vapour loss shapes planetary compositions. Nature 549, 511–515.
Hofmann, A., 1971. Fractionation corrections for mixed-isotope spikes of Sr, K, and Pb. Earth Planet. Sci. Lett. 10, 397–402.
Hu, Y., Teng, F.-Z., Zhang, H.-F., Xiao, Y., Su, B.-X., 2016. Metasomatism-induced mantle magnesium isotopic heterogeneity: Evidence from pyroxenites. Geochim. Cosmochim. Acta 185, 88–111.
Hu, Y., Teng, F.-Z., Ionov, D.A., 2020. Magnesium isotopic composition of metasomatized upper sub-arc mantle and its implications to Mg cycling in subduction zone. Geochim. Cosmochim. Acta 278, 219–234.
Huang, F., Zhang, Z., Lundstrom, C.C., Zhi, X., 2011. Iron and magnesium isotopic compositions of peridotite xenoliths from Eastern China. Geochim. Cosmochim. Acta 75, 3318–3334.
Huang, F., Chen, L.-J., Wu, Z.-Q., Wang, W., 2013. First-principles calculations of equilibrium Mg isotope fractionations between garnet, clinopyroxene, orthopyroxene, and olivine: Implications for Mg isotope thermometry. Earth Planet. Sci. Lett. 367, 61–70.
Huang, F., Wu, Z., Huang, S., Wu, F., 2014. First-principles calculations of equilibrium silicon isotope fractionation among mantle minerals. Geochim. Cosmochim. Acta 140, 509–520.
Ionov, D.A., 2004. Chemical variations in peridotite xenoliths from Vitim, Siberia: Inference for REE and Hf behaviour in the Garnet-Facies Upper Mantle. J. Petrol. 45, 343–367.
Ionov, D.A., 2007. Compositional variations and heterogeneity in fertile lithospheric mantle: peridotite xenoliths in basalts from Tariat, Mongolia. *Contrib. Mineral. Petrol.* 154, 455–477.
Ionov, D.A., 2010. Petrology of mantle wedge lithosphere: new data on supra-subduction zone peridotite xenoliths from the andesitic Avacha volcano, Kamchatka. *J. Petrol.* 51, 327–361.
Ionov, D.A., Hofmann, A.W., 2007. Depth of formation of subcontinental off-craton peridotites. Earth Planet. Sci. Lett. 261, 620–634.
Ionov, D.A., Bénard, A., Plechov, P.Y., 2011. Melt evolution in subarc mantle: Evidence from heating experiments on spinel-hosted melt inclusions in peridotite xenoliths from the andesitic Avacha volcano (Kamchatka, Russia). Contrib. Miner. Petrol. 162, 1159–1174.
Ionov, D.A., Seitz, H.M., 2008. Lithium abundances and isotopic compositions in mantle xenoliths from subduction and intra-plate settings: Mantle sources vs. eruption histories. Earth Planet. Sci. Lett. 266, 316–331.
Ionov, D.A., Ashchepkov, I., Jagoutz, E., 2005. The provenance of fertile off-craton lithospheric mantle: Sr–Nd isotope and chemical composition of garnet and spinel peridotite xenoliths from Vitim, Siberia. *Chem. Geol.* 217, 41–75.
Johnson, K.T., Dick, H.J., Shimizu, N., 1990. Melting in the oceanic upper mantle: An ion microprobe study of diopsides in abyssal peridotites. J. Geophys. Res. Solid Earth 95, 2661–2678.
Klaver, M., Ionov, D.A., Takazawa, E., Elliott, T., 2020. The non-chondritic Ni isotope composition of Earth's mantle. Geochim. Cosmochim. Acta 268, 405–421.
Klein, E.M., Langmuir, C.H., 1987. Global correlations of ocean ridge basalt chemistry with axial depth and crustal thickness. J. Geophys. Res. Solid Earth 92, 8089–8115.
Lai, Y.-J., Pogge von stranmann, P.A.E., Dohmen, R., Takazawa, E., Elliott, T., 2015. The influence of melt infiltration on the Li and Mg isotopic composition of the Horoman peridotite massif. Geochim. Cosmochim. Acta 164, 318–332.
Lehmann, J., 1983. Diffusion between olivine and spinel: Application to geothermometry. Earth Planet. Sci. Lett. 64, 123–138.
Liermann, H.P., Ganguly, J., 2002. Diffusion kinetics of Fe^{2+} and Mg in aluminous spinel: Experimental determination and applications. Geochim. Cosmochim. Acta 66, 2903–2913.
Liu, X.-N., Hin, R.C., Coath, C.D., van Soest, M., Melekhova, E., Elliott, T., 2022. Equilibrium olivine-melt Mg isotopic fractionation explains high δ^{26}Mg values in arc lavas. Geochem. Persp. Let. 22, 42–47.
Liu, S.-A., Teng, F.-Z., Yang, W., Wu, F.-Y., 2011. High-temperature inter-mineral magnesium isotope fractionation in mantle xenoliths from the North China craton. Earth Planet. Sci. Lett. 308, 255–270.
Liu, P.-P., Teng, F.-Z., Dick, H.J.B., Zhou, M.-F., Chung, S.-L., 2017. Magnesium isotopic composition of the oceanic mantle and oceanic Mg cycling. Geochim. Cosmochim. Acta 206, 151–165.
Luu, T.H., Hin, R.C., Coath, C.D., Elliott, T., 2019. Bulk chondrite variability in mass independent magnesium isotope compositions–Implications for initial solar system $^{26}Al/^{27}Al$ and the timing of terrestrial accretion. Earth Planet. Sci. Lett. 522, 166–175.
Malaviarachchi, S.P.K., Makishima, A., Tanimoto, M., Kuritani, T., Nakamura, E., 2008. Highly unradiogenic lead isotoperatios from the Horoman peridotite in Japan. Nat. Geosci. 1, 859–863.
Malaviarachchi, S.P.K., Makishima, A., Nakamura, E., 2010. Melt-peridotite reactions and fluid metasomatism in the upper mantle, revealed from the geochemistry of peridotite and gabbro from the Horoman Peridotite Massif, Japan. *J. Petrol.* 51, 1417–1445.
Malpas, J., Zhou, M.-F., Robinson, P.T., Reynolds, P.H., 2003. Geochemical and geochronological constraints on the origin and emplacement of the Yarlung Zangbo ophiolites, Southern Tibet. Geol. Soc., Lond. 218, 191–206.
Oeser, M., Dohmen, R., Horn, I., Schuth, S., Weyer, S., 2015. Processes and time scales of magmatic evolution as revealed by Fe–Mg chemical and isotopic zoning in natural olivines. Geochim. Cosmochim. Acta 154, 130–150.
Ozawa, K., 1983. Evaluation of olivine-spinel geothermometry as an indicator of thermal history for peridotites. Contrib. Miner. Petrol. 82, 52–65.
Palme, H., O'Neill, H., 2014. Cosmochemical estimates of mantle composition. In: Holland, H.D., Turekian, K.K. (Eds.), Treatise on Geochemistry, second ed. Elsevier, Oxford, pp. 1–39.
Petermann, M., Hirschmann, M.M., 2003. Anhydrous partial melting experiments on MORB-like Eclogite: Phase relations, phase compositions and mineral-melt partitioning of major elements at 2–3 GPa. J. Petrol. 44, 2173–2201.
Petrini, R., Joron, J.L., Ottonello, G., Bonatti, E., Seyler, M., 1988. Basaltic dykes from Zabargad Island, Red Sea: Petrology and geochemistry. Tectonophysics 150, 229–248.
Pogge von Strandmann, P., Elliott, T., Marschall, H.R., Coath, C., Lai, Y.-J., Jeffcoate, A. B., Ionov, D.A., 2011. Variations of Li and Mg isotope ratios in bulk chondrites and mantle xenoliths. Geochim. Cosmochim. Acta 75, 5247–5268.
Preß, S., Witt, G., Seck, H.A., Eonov, D., Kovalenko, V.I., 1986. Spinel peridotite xenoliths from the Tariat Depression, Mongolia. I: Major element chemistry and mineralogy of a primitive mantle xenolith suite. Geochim. Cosmochim. Acta 50, 2587–2599.
Ramsey, S.R., Howarth, G.H., Udry, A., Gross, J., 2021. Nickel–manganese variability in olivine and Al-in-olivine thermometry for olivine-phyric shergottites. Meteorit. Planet. Sci. 56, 1597–1618.
Robinson, C.J., Wood, B.J., Blundy, J.D., 1998. The beginning of melting of fertile and depleted peridotite at 1.5 GPa. Earth Planet. Sci. Lett. 155, 97–111.
Roeder, P.L., Campbell, I.H., Jamieson, H.E., 1979. A re-evaluation of the olivine-spinel geothermometer. Contrib. Miner. Petrol. 68, 325–334.
Rudge, J.F., Reynolds, B.C., Bourdon, B., 2009. The double spike toolbox. Chem. Geol. 265, 420–431.
Saal, A.E., Takazawa, E., Frey, F.A., Shimizu, N., Hart, S.R., 2001. Re–Os isotopes in the Horoman peridotite: evidence for refertilization? J. Petrol. 42, 25–37.
Schauble, E.A., 2011. First-principles estimates of equilibrium magnesium isotope fractionation in silicate, oxide, carbonate and hexaaquamagnesium(2+) crystals. Geochim. Cosmochim. Acta 75, 844–869.
Sen, G., 1988. Petrogenesis of spinel lherzolite and pyroxenite suite xenoliths from the Koolau shield, Oahu, Hawaii: Implications for petrology of the post-eruptive lithosphere beneath Oahu. Contrib. Miner. Petrol. 100, 61–91.
Sen, G., Frey, F.A., Shimizu, N., Leeman, W.P., 1993. Evolution of the lithosphere beneath Oahu, Hawaii: Rare earth element abundances in mantle xenoliths. Earth Planet. Sci. Lett. 119, 53–69.
Shaw, D.M., 2006. Trace Elements in Magmas. Cambridge University Press, New York.
Sio, C.K.I., Dauphas, N., Teng, F.-Z., Chaussidon, M., Helz, R.T., Roskosz, M., 2013. Discerning crystal growth from diffusion profiles in zoned olivine by in situ Mg–Fe isotopic analyses. Geochim. Cosmochim. Acta 123, 302–321.
Soderman, C.R., Shorttle, O., Matthews, S., Williams, H.M., 2022. Global trends in novel stable isotopes in basalts: Theory and observations. Geochim. Cosmochim. Acta 318, 388–414.
Steele, R.C.J., Coath, C.D., Regelous, M., Russell, S., Elliott, T., 2012. Neutron-poor Nickel isotope anomalies in meteorites. Astrophys. J. 758, 59–80.
Stosch, H.G., Lugmair, G.W., Kovalenko, V.I., 1986. Spinel peridotite xenoliths from the Tariat Depression, Mongolia. II: Geochemistry and Nd and Sr isotopic composition and their implications for the evolution of the subcontinental lithosphere. Geochim. Cosmochim. Acta 50, 2601–2614.
Stracke, A., Tipper, E.T., Klemme, S., Bizimis, M., 2018. Mg isotope systematics during magmatic processes: Intermineral fractionation in mafic to ultramafic Hawaiian xenoliths. Geochim. Cosmochim. Acta 226, 192–205.
Su, B.-X., Teng, F.-Z., Hu, Y., Shi, R.-D., Zhou, M.-F., Zhu, B., Liu, F., Gong, X.-H., Huang, Q.-S., Xiao, Y., Chen, C., 2015. Iron and magnesium isotope fractionation in oceanic lithosphere and sub-arc mantle: Perspectives from ophiolites. Earth Planet. Sci. Lett. 430, 523–532.

Takazawa, E., Frey, F., Shimizu, N., Obata, M., 1996. Evolution of the Horoman Peridotite (Hokkaido, Japan): Implications from pyroxene compositions. Chem. Geol. 134, 3–26.
Takazawa, E., Frey, F., Shimizu, N., Obata, M., 2000. Whole rock compositional variations in an upper mantle peridotite (Horoman, Hokaido, Japan): Are they consistent with a partial melting process? Geochim. Cosmochim. Acta 64, 695–716.
Teng, F.-Z., 2017. Magnesium isotope geochemistry. Rev. Mineral. Geochem. 82, 219–287.
Teng, F.-Z., Li, W.-Y., Ke, S., Marty, B., Dauphas, N., Huang, S., Wu, F.-Y., Pourmand, A., 2010. Magnesium isotopic composition of the Earth and chondrites. Geochim. Cosmochim. Acta 74, 4150–4166.
Teng, F.-Z., Dauphas, N., Helz, R.T., Gao, S., Huang, S., 2011. Diffusion-driven magnesium and iron isotope fractionation in Hawaiian olivine. Earth Planet. Sci. Lett. 308, 317–324.
Teng, F.-Z., Li, W.-Y., Ke, S., Yang, W., Liu, S.-A., Sedaghatpour, F., Wang, S.-J., Huang, K.-J., Hu, Y., Ling, M.-X., Xiao, Y., Liu, X.-M., Li, X.-W., Gu, H.-O., Sio, C.K., Wallace, D.A., Su, B.-X., Zhao, C., Harrington, J., Brewer, M.A., 2015a. Magnesium isotopic compositions of international geological reference materials. Geostand. Geoanalyt. Res. 39, 329–339.
Teng, F.-Z., Yang, W., 2014. Comparison of factors affecting the accuracy of high-precision magnesium isotope analysis by multi-collector inductively coupled plasma mass spectrometry. Rapid Commun. Mass Spectrom. 28, 19–24.
Teng, F.-Z., Yin, Q.-Z., Ullmann, C.V., Chakrabarti, R., Pogge von Strandmann, P.A.E., Yang, W., Li, W.-Y., Ke, S., Sedaghatpour, F., Wimpenny, J., Meixner, A., Romer, R. L., Wiechert, U., Jacobsen, S.B., 2015b. Interlaboratory comparison of magnesium isotopic compositions of 12 felsic to ultramafic igneous rock standards analyzed by MC-ICPMS. Geochem. Geophys. Geosyst. 16, 3197–3209.
Walter, M.J., 1998. Melting of garnet peridotite and the origin of komatiite and depleted lithosphere. J. Petrol. 29, 29–60.
Wan, Z., Coogan, L.A., Canil, D., 2008. Experimental calibration of aluminum partitioning between olivine and spinel as a geothermometer. Am. Min. 93, 1142–1147.
Wang, X.-J., Chen, L.-H., Hofmann, A.W., Hanyu, T., Kawabata, H., Zhong, Y., Xie, L.-W., Shi, J.-H., Miyazaki, T., Hirahara, Y., Takahashi, T., Senda, R., Chang, Q., Vaglarov, B.S., Kimura, J.-I., 2018. Recycled ancient ghost carbonate in the Pitcairn mantle plume. Proc. Natl. Acad. Sci. 115, 8682–8687.
Wang, Y., He, Y.-S., Ke, S., 2020. Mg isotope fractionation during partial melting of garnet-bearing sources: An adakite perspective. Chem. Geol. 537, 119478.
Wang, S.-J., Teng, F.-Z., Scott, J.M., 2016. Tracing the origin of continental HIMU-like intraplate volcanism using magnesium isotope systematics. Geochim. Cosmochim. Acta 185, 78–87.
Williams, H.M., Bizimis, M., 2014. Iron isotope tracing of mantle heterogeneity within the source regions of oceanic basalts. Earth Planet. Sci. Lett. 404, 396–407.
Williams, H.M., Matthews, S., Rizo, H., Shorttle, O., 2021. Iron isotopes trace primordial magma ocean cumulates melting in Earth's upper mantle. Sci. Adv. 7, eabc7394.
Wu, Z., Huang, F., Huang, S., 2015. Isotope fractionation induced by phase transformation: First-principles investigation for Mg_2SiO_4. Earth Planet. Sci. Lett. 409, 339–347.
Xiao, Y., Teng, F.-Z., Zhang, H.-F., Yang, W., 2013. Large magnesium isotope fractionation in peridotite xenoliths from eastern North China craton: Product of melt–rock interaction. Geochim. Cosmochim. Acta 115, 241–261.
Xiao, Y., Teng, F.-Z., Su, B.-X., Hu, Y., Zhou, M.-F., Zhu, B., Shi, R.-D., Huang, Q.-S., Gong, X.-H., He, Y.-S., 2016. Iron and magnesium isotopic constraints on the origin of chemical heterogeneity in podiform chromitite from the Luobusa ophiolite, Tibet. Geochem. Geophys. Geosyst. 17, 940–953.
Yang, W., Teng, F.-Z., Zhang, H.-F., 2009. Chondritic magnesium isotopic composition of the terrestrial mantle: A case study of peridotite xenoliths from the North China craton. Earth Planet. Sci. Lett. 288, 475–482.
Yoshikawa, M., Nakamura, E., 2000. Geochemical evolution of the Horoman peridotite complex: Implications for melt extraction, metasomatism, and compositional layering in the mantle. J. Geophys. Res. Solid 105, 2879–2901.
Yoshikawa, M., Nakamura, E., Takahashi, N., 1993. Rb–Sr isotope systematics in a phlogopite-bearing spinel lherzolite and its implications for age and origin of metasomatism in the Horoman peridotite complex, Hokkaido, Japan. *J. Mineral. Petrol. Econ. Geol.* 88, 121–130.
Young, E.D., Tonui, E., Manning, C.E., Schauble, E., Macris, C.A., 2009. Spinel–olivine magnesium isotope thermometry in the mantle and implications for the Mg isotopic composition of Earth. Earth Planet. Sci. Lett. 288, 524–533.
Zhao, X.-M., Ca, H.-H., Mi, X., Evans, N.J., Qi, Y.-H., Huang, F., Zhang, H.-F., 2017. Combined iron and magnesium isotope geochemistry of pyroxenite xenoliths from Hannuoba, North China Craton, implication for mantle metasomatism. Contrib. Mineral. Petri. 172, 40.
Zhao, M.-S., Chen, Y.-X., Xiong, J.-W., Zheng, Y.-F., Zha, X.-P., Huang, F., 2023. Element mobility and Mg isotope fractionation during peridotite serpentinization. Geochim. Cosmochim. Acta 340, 21–37.
Zhao, X.-M., Zhang, H.-F., Zhu, X.-K., Tang, S.-H., Yan, B., 2012. Iron isotope evidence for multistage melt-peridotite interactions in the lithospheric mantle of eastern China. Chem. Geol. 292–293, 127–139.
Zhong, Y., Chen, L.-H., Wang, X.-J., Zhang, G.-L., Xie, L.-W., Zeng, G., 2017. Magnesium isotopic variation of oceanic island basalts generated by partial melting and crustal recycling. Earth Planet. Sci. Lett. 463, 127–135.